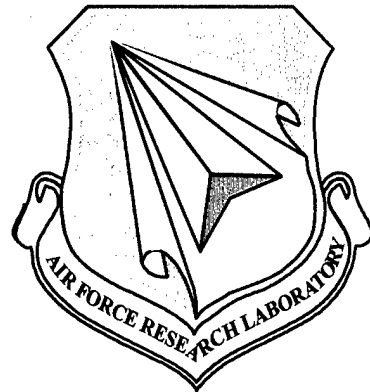


AFRL-MN-EG-TR-2000-7005

Investigation of Interface Resolution Techniques in Moving Boundary Problems

W. Shyy
H.S. Udaykumar

University Of Florida
Dept. of Aerospace Engineering, Mechanics
and Engineering Science
Gainesville, Florida 32611



D. Belk
K. Vanden

Air Force Research Laboratory
Munitions Directorate
Computational Mechanics Branch (AFRL/MNAC)
Eglin AFB, FL 32542-6810

GRANT NO. FO8630-97-1-0002

January 2000

FINAL REPORT FOR PERIOD August 1997 - September 1999

20000417 139

DISTRIBUTION A. Approved for public release; distribution unlimited.

AIR FORCE RESEARCH LABORATORY, MUNITIONS DIRECTORATE

Air Force Materiel Command n United States Air Force n Eglin Air Force Base

DTIC QUALITY INSPECTED 3

REPORT DOCUMENTATION PAGE

Form Approved
OMB No. 0704-0188

Public reporting burden for this collection of information is estimated to average 1 hour per response, including the time for reviewing instructions, searching existing data sources, gathering and maintaining the data needed, and completing and reviewing the collection of information. Send comments regarding this burden estimate or any other aspect of this collection of information, including suggestions for reducing this burden, to Washington Headquarters Services, Directorate for Information Operations and Reports, 1215 Jefferson Davis Highway, Suite 1204, Arlington, VA 22202-4302, and to the Office of Management and Budget, Paperwork Reduction Project (0704-0188), Washington, DC 20503.

1. AGENCY USE ONLY (Leave blank)

2. REPORT DATE
January 2000

3. REPORT TYPE AND DATES COVERED
Final August 1997 – September 1999

4. TITLE AND SUBTITLE

Investigation of Interface Resolution Techniques in Moving Boundary Problems.

5. FUNDING NUMBERS

Grant #: FO8630-97-1-0002
JON: 25020725 PE:62602F
PR:2502
TA:07
WU:25

6. AUTHOR(S) W. Shyy, H.S. Udaykumar, D. Belk, and K. Vanden

7. PERFORMING ORGANIZATION NAME(S) AND ADDRESS(ES)

University Of Florida
Dept. of Aerospace Engineering, Mechanics
and Engineering Science
Gainesville, Florida 32611
USAF Research Laboratory
Computational Mechanics Branch
101 W. Eglin Blvd, Ste #337
Eglin AFB, Florida 32542-6810

8. PERFORMING ORGANIZATION REPORT
NUMBER

9. SPONSORING/MONITORING AGENCY NAME(S) AND ADDRESS(ES) (Program Mgr Name & Ph #)

USAF Research Laboratory
Computational Mechanics Branch (AFRL/MNAC)
101 W. Eglin Blvd, Ste #337
Eglin AFB, Florida 32542-6810

10. SPONSORING/MONITORING AGENCY
REPORT NUMBER

AFRL-MN-EG-TR-2000-7005

Program Manager: Dr Kirk Vanden, 850-882-3124 (x3351)

11. SUPPLEMENTARY NOTES

Availability of this report is specified on the verso of front cover.

12a. DISTRIBUTION/AVAILABILITY STATEMENT

DISTRIBUTION A. Approved for public release; distribution unlimited.

12b. DISTRIBUTION CODE

13. ABSTRACT:

In this report we describe the development of a numerical solution technique for the simulation of high-speed multi-material impact. Of particular interest is the interaction of solid impactors with targets. Such interactions present the following challenges to numerical solution techniques: 1.) high velocities of impact leading to large deformations of the impactor as well as the targets. 2) nonlinear wave-propagation and the development of shocks in the system. 3) Modeling of the constitutive properties of materials under intense impact conditions and accurate numerical calculation of the elasto-plastic behavior described by the models 4) Phenomena at multiple interfaces such as impactor-target, target-ambient and impactor-ambient. It is demonstrated that the interface can be tracked through large distortions. Accurate shock-capturing schemes can be implemented for cartesian grids and extended to incorporate the presence of the moving interfaces. Computations of the deformation process are carried to large distortions while the interfaces travel through the mesh in a stable and robust manner. The solution algorithms used in this study were developed primarily at the Air Force Research Laboratory, while the interface resolution and tracking portion of this effort was developed at the University of Florida.

14. SUBJECT TERM ENO shock capturing hydrocode finite-volume elastic plastic impact

I

15. NUMBER OF PAGES
46

16. PRICE CODE

17. SECURITY CLASSIFICATION OF
REPORT
UNCLASSIFIED

18. SECURITY CLASSIFICATION
OF THIS PAGE
UNCLASSIFIED

19. SECURITY CLASSIFICATION
OF ABSTRACT
UNCLASSIFIED

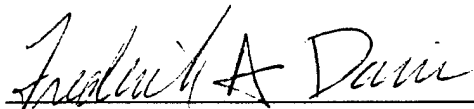
20. LIMITATION OF ABSTRACT
SAR

NOTICE

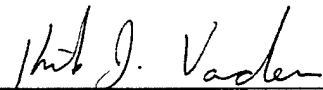
When Government drawings, specifications, or other data are used for any purpose other than in connection with a definitely Government-related procurement, the United States Government incurs no responsibility or any obligation whatsoever. The fact that the Government may have formulated or in any way supplied the said drawings, specifications, or other data, is not to be regarded by implication, or otherwise in any manner construed, as licensing the holder, or any other person or corporation; or as conveying any rights or permission to manufacture, use, or sell any patented invention that may in any way be related thereto.

This technical report is releasable to the National Technical Information Services (NTIS). At NTIS it will be available to the general public, including foreign nations.

This technical report has been reviewed and is approved for publication.



FREDERICK A DAVIS, Technical Director
Assessment and Demonstrations Division



Dr Kirk Vanden
Program Manager

If your address has changed, if you wish to be removed from our mailing list, or if your organization no longer employs the addressee, please notify AFRL/MNAC, Eglin AFB FL 32542-6810, to help us maintain a current mailing list.

Do not return copies of this report unless contractual obligations or notice on a specific document requires that it be returned.

PREFACE

The work presented in this technical report was a joint effort between researchers at the Air Force Research Laboratory (AFRL) and the University of Florida. The Computational Mechanics Branch (AFRL/MNAC) was the primary developer of the high order ENO solution algorithm for the governing equations of uniaxial strain (1D) and plane strain (2D). The University of Florida developed and implemented the interface resolution and tracking algorithms.

1. Introduction

The dynamics of high-speed impact between materials is characterized by large deformation and short time scales. Wave propagation in the impacting media is highly nonlinear, and involves localized phenomena such as shear bands, crack propagation, and wave refraction (Meyers, 1994). These problems are typically challenging to solve because, in contrast to conventional structural dynamics problems, the deviatoric and pressure terms in the stress tensors are both important and need to be modeled separately. In contrast to conventional fluid dynamics problems, the stress and strain fields are related through nonlinear elasto-plastic yield surfaces, the models for which must be included in the governing equations. Furthermore, the interface between materials experiences not only fast motion, but also large variations in shape. Such problems have been routinely handled by the so-called hydrocodes. Benson (1992) provides a very detailed review of the formulation, modeling and computational techniques employed by these large-scale computer codes.

In the past several years, progress has been made toward developing predictive techniques based on the application of modern computational solid and fluid dynamics. For example, Camacho and Ortiz (1996, 1997) have developed a Lagrangian finite element impact dynamics model involving brittle materials (Camacho and Ortiz 1996), and ductile penetration (Camacho and Ortiz 1997). Their approach is based on adaptive meshing, explicit contact/friction algorithm, and rate dependent plasticity. Trangenstein (1990, 1994, 1995), and Trangenstein and Pember (1991) have adopted Godunov's method and ideas developed in modern computational fluid dynamics to handle the problem in the context of a Riemann type problem with second-order accuracy. In addition, there have also been finite volume methods based on general discretization treatments (Bailey and Cross 1995, Dormy and Tarantola 1995) with first-order accuracy.

Overall, it seems clear that while progress has been made, impact dynamics has been rigorously investigated only recently. Much remains to be done before we can treat it satisfactorily in terms of geometric representation, interface movement, temporal and spatial resolution, accuracy of numerical schemes and incorporation of realistic materials behavior models.

In this report we describe the development of a numerical solution technique for the simulation of high-speed multimaterial impact. Of particular interest is the interaction of solid impactors with targets. This problem is important in applications such as munition-target interactions, geological impact dynamics, shock processing, and formation of shaped charges upon detonation and their subsequent interaction with targets (Meyers, 1994). Such interactions present the following challenges to numerical simulation techniques:

1. High velocities of impact leading to large deformations of the impactor as well as targets.
2. Nonlinear wave-propagation and the development of shocks in the systems.
3. Modeling of the constitutive properties of materials under intense impact conditions and accurate numerical calculation of the elastic-plastic behavior described by the models.
4. Phenomena at multiple interfaces (such as impactor-target, target-ambient and impactor-ambient), i.e. both free surface and surface-surface dynamics.

This report describes a numerical approach that seeks to tackle all of the above aspects. In the following description we elaborate on the numerical framework for solution of high-velocity impact problems and present a rationale for choice of the numerical methodology. We also address issues of accuracy in the treatment of the wave propagation in the bulk media and interactions at the interfaces, and present results showing the capability of the method.

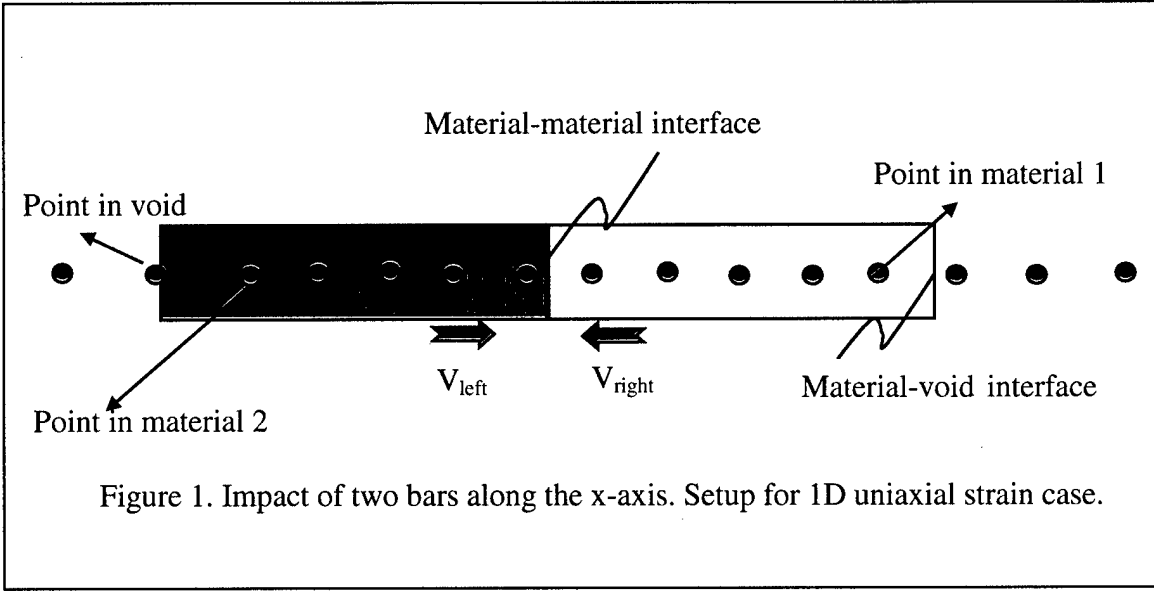
2. Governing Equations for 1D case: Uniaxial strain

The system being simulated in the 1D case is as shown in Figure 1. We consider two slender rods impacting on the x-axis. The rods can be of finite or infinite extent. The system of governing equations for the elastic-plastic flow under uniaxial strain conditions is of the form:

$$\frac{\partial \bar{Q}}{\partial t} + \frac{\partial F(\bar{Q})}{\partial x} = S(\bar{Q}) \quad (1)$$

Where the vector of dependent variables \bar{Q} is

$$\bar{Q} = \begin{bmatrix} q_1 \\ q_2 \\ q_3 \\ q_4 \\ q_5 \end{bmatrix} = \begin{bmatrix} \rho \\ \rho u \\ E \\ \rho \bar{\epsilon} \\ \rho s_x \end{bmatrix} \quad (2)$$



where ρ is the density, u is the velocity, E is energy, $\bar{\epsilon}$ is the equivalent plastic strain, s_x is the deviatoric stress.

The flux vector is of the form

$$F(\vec{Q}) = \begin{bmatrix} \rho u \\ \rho u^2 + p \\ u(E + p) \\ \rho u \bar{\epsilon} \\ \rho u s_x \end{bmatrix} \quad (3)$$

where p is the pressure. The source vector is

$$S(\vec{Q}) = \begin{bmatrix} 0 \\ \frac{\partial s_x}{\partial x} \\ \frac{\partial (u s_x)}{\partial x} \\ S_{\bar{\epsilon}} \\ S_{s_x} \end{bmatrix} \quad (4)$$

Here

$$S_{s_x} = \left(1 - \frac{1}{1 + H'/3G}\right) \frac{4G}{3} \rho \frac{\partial u}{\partial x} \quad (5)$$

and

$$S_{\bar{\epsilon}} = \left(\frac{1}{1 + H'/3G} \right) \frac{2\rho}{3} \left| \frac{\partial u}{\partial x} \right| \quad (6)$$

are the source terms arising in the equations for deviatoric stress and equivalent plastic strain. G is the shear modulus of the material and $\sigma_e = H(\bar{\epsilon})$ is the equivalent stress-strain curve as determined by uniaxial strain experiments. The pressure is determined by an equation of state (eos) of the form:

$$p = eos(\rho, \rho u^2, E) \quad (7)$$

The specific eos in use here is the Mie-Gruneisen eos (Meyers 1994):

$$p(e_i, V) = \frac{c_0^2 (V_0 - V)}{[V_0 - s(V_0 - V)]^2} + \frac{\Gamma(V)}{V} \left[e_i - \frac{1}{2} \left(\frac{c_0 (V_0 - V)}{V_0 - s(V_0 - V)} \right)^2 \right] \quad (8)$$

where

$$e_i = \frac{E}{\rho} - \frac{u^2}{2} \quad (9)$$

$$V = \frac{1}{\rho} \quad (10)$$

and

$$\Gamma = V \left(\frac{\partial p}{\partial e_i} \right) = \frac{\Gamma_0 \rho_0}{\rho} \quad (11)$$

where ρ_0 is the density of the unstressed material, c_0 and s are coefficients that relate the shock speed U_s and the particle velocity:

$$U_s = c_0 + su \quad (12)$$

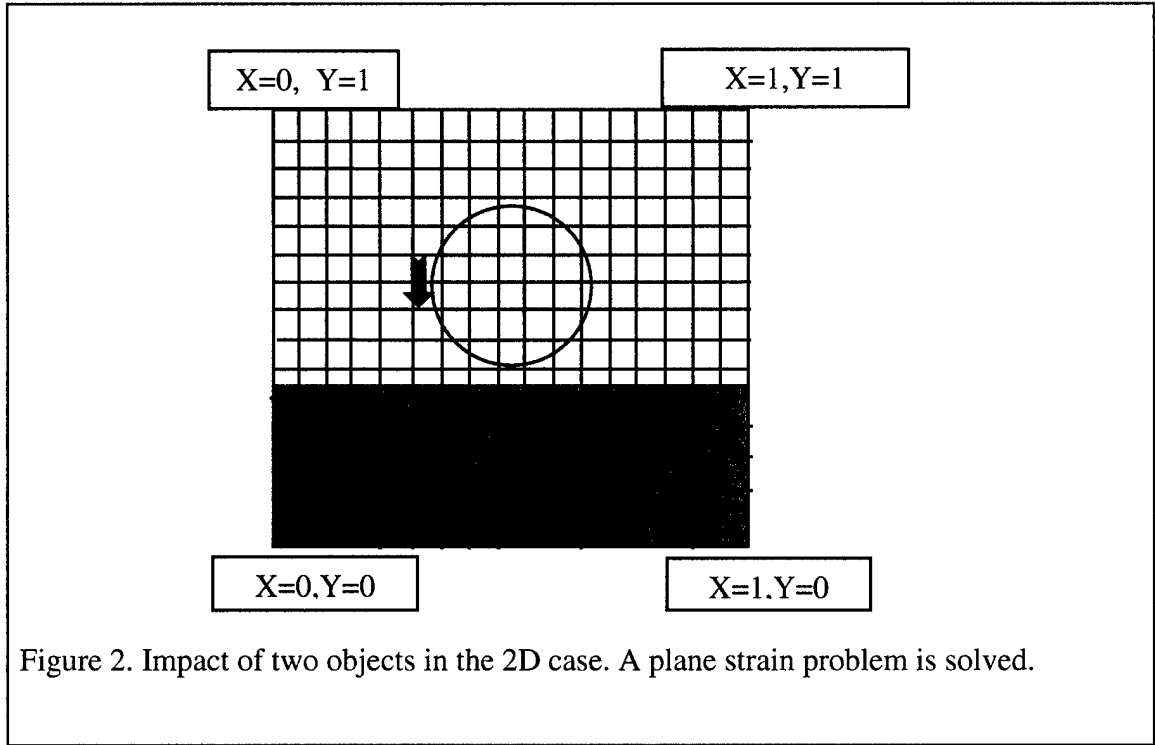
The conditions that apply at the ends of the rods depend on the extent of the rods and are addressed later in this report.

3. Governing equations for the 2D case: Plane strain

In 2D the impact of arbitrary shapes can be considered in the plane as illustrated in Figure 2. The equations in 2D correspond to the plane-strain situation and are as follows:

The transport equation in vector form is:

$$\frac{\partial \vec{Q}}{\partial t} + \frac{\partial F(\vec{Q})}{\partial x} + \frac{\partial G(\vec{Q})}{\partial y} = S(\vec{Q}) \quad (13)$$



The vector of independent variables, and the x- and y-direction convective flux vectors are given by:

$$\bar{Q} = \begin{bmatrix} q_1 \\ q_2 \\ q_3 \\ q_4 \\ q_5 \\ q_6 \\ q_7 \\ q_8 \end{bmatrix} = \begin{bmatrix} \rho \\ \rho u \\ \rho v \\ E \\ \bar{\epsilon} \\ s_{xx} \\ s_{yy} \\ s_{xy} \end{bmatrix} \quad (14a)$$

$$F(\bar{Q}) = \begin{bmatrix} \rho u \\ \rho u^2 \\ \rho uv \\ uE \\ u\bar{\epsilon} \\ us_{xx} \\ us_{yy} \\ us_{xy} \end{bmatrix} \quad (14b)$$

$$G(\vec{Q}) = \begin{bmatrix} \rho v \\ \rho v u \\ \rho v^2 \\ v E \\ v \bar{\epsilon} \\ v s_{xx} \\ v s_{yy} \\ v s_{xy} \end{bmatrix} \quad (14c)$$

The source vector is:

$$S(\vec{Q}) = \begin{bmatrix} 0 \\ \frac{\partial \sigma_{xx}}{\partial x} + \frac{\partial \sigma_{xy}}{\partial y} \\ \frac{\partial \sigma_{xy}}{\partial x} + \frac{\partial \sigma_{yy}}{\partial y} \\ \frac{\partial (u \sigma_{xx} + v \sigma_{xy})}{\partial x} + \frac{\partial (u \sigma_{xy} + v \sigma_{yy})}{\partial y} \\ S_{\bar{\epsilon}} \\ S_{s_{xx}} \\ S_{s_{yy}} \\ S_{s_{xy}} \end{bmatrix} \quad (15)$$

where the source term in the equation for equivalent plastic strain is:

$$S_{\bar{\epsilon}} = \left(\frac{1}{1 + H' / 3G} \right) \frac{s_{ij} D'_{ij}}{\bar{\sigma}} + \bar{\epsilon} \frac{\partial u}{\partial x} + \bar{\epsilon} \frac{\partial v}{\partial y} \quad (16a)$$

In this and other expressions where the tensor index notation is mixed with Cartesian component notation, subscripts 1,2 or 3 correspond to x,y or z respectively. The source term in the equation for deviatoric stress component is:

$$S_{s_{ij}} = 2G \left[D'_{ij} - \frac{3}{2} \frac{s_{ij} s_{mn}}{\bar{\sigma}^2} \frac{D'_{mn}}{1 + \frac{H'}{3G}} \right] - \Omega_{ik} S_{kj} + S_{ik} \Omega_{kj} + S_{ij} \frac{\partial u}{\partial x} + S_{ij} \frac{\partial v}{\partial y} \quad (16b)$$

In the above the rate of deformation tensor components D_{ij} are used and these are defined as

$$D'_{ij} = D_{ij} - \frac{1}{3} D_{kk} \delta_{ij} \quad (17a)$$

$$D_{ij} = \frac{1}{2} \left[\frac{\partial u_i}{\partial x_j} + \frac{\partial u_j}{\partial x_i} \right] \quad (17b)$$

$$\Omega_{ij} = \frac{1}{2} \left[\frac{\partial u_i}{\partial x_j} - \frac{\partial u_j}{\partial x_i} \right] \quad (17c)$$

where δ_{ij} is the Kronecker delta. The terms in Equation (16b) that involve Ω are needed to maintain material frame indifference.

In the equation set above the three components of deviatoric stress are chosen as the dependent variables. The total stress components are related to the deviatoric stresses as:

$$\sigma_{ij} = s_{ij} - p \delta_{ij} \quad (18)$$

where by definition $p = -\frac{1}{3} \sigma_{kk}$.

In addition, one again requires the eos for the pressure which is given by the Mie-Gruneisen equation of state, Eq. (8). The above set of equations is solved in the presence of moving boundaries, namely the impactor and target. The numerical approach adopted for solving the governing equations needs to incorporate the presence of these moving boundaries where various types of boundary conditions may apply. Therefore the critical issue of the manner in which interfacial dynamics is approached numerically is addressed next.

4. Numerical Approaches for Moving Boundary Problems in Fluid Mechanics

A large variety of physical phenomena involve the coupling of evolution of flowfields or material deformation fields with boundaries that move, deform or evolve in time. Examples include the deformation of drops, bubbles, liquid free surfaces etc., the evolution of phase boundaries in solidification and vaporization, fluid-structure interaction problems at the large scale such as in aeroelasticity, and in the small scale such as in biomechanics and a whole host of other interesting phenomena. These problems are challenging to CFD practitioners due to the complexity associated with the often severely deformed boundaries in (or enclosing) the flow, and the nonlinearity resulting from the coupling of the interface dynamics with the dynamics of the flowfield. Ideally one would like to track the moving boundary as a sharp front (assuming discontinuities in some flow quantity such as stress, energy etc. are present across the interface) without smearing information at the front. Also, one would like to solve the flowfield within the regions separated by the interfaces with desired accuracy. If the interfaces become multiply connected one would wish to follow the

evolution of the interfaces through such topological changes. Of course, it would also be desirable to correctly model the physics so that all the ingredients of the dynamics can be included in the model. Algorithms for computational solution of moving boundary problems operate under these demands.

In the computational fluid dynamics literature numerous methods have been developed for the purpose of handling moving boundary interaction with flows. These can be classed broadly under the categories of Eulerian, Lagrangian and mixed (Eulerian-Lagrangian) methods. We will briefly summarize the salient features of each method in the following:

1. Lagrangian methods: Ideally one would want to simulate the effect of the boundary by treating it explicitly, without smearing the information at the interface, i.e. with minimum numerical diffusion. There are several ways of doing this. For a fixed boundary, when the shape is truly complex, one can resort to block-structured domain decomposition (Shyy, 1994), overset meshes (Steger, 1999, Johnson and Belk, 1995), or unstructured boundary-conforming curvilinear grids (Venkatakrishnan, 1996) to discretize the domain. The last method has been developed very strongly by the finite-element community (Camacho and Ortiz, 1996, 1997) and has been used also by the fluid dynamics community (Fritz and Boris, 1979, Glimm et al., 1988, Rausch et al., 1993) for moving boundary problems. There has also been an emergence of meshless methods for the solution of finite deformation problems (Liszka et al., 1996, Duarte et al., 1996, Randles et al., 1996). These have been successful in solving an impressive array of problems. For moving boundaries which may undergo large deformations, or are subject to topology changes in the course of their evolution, generating body-fitted grids to conform to complex boundaries may become taxing. Furthermore, as will be elaborated below there are certain advantages to solving large distortion problems on fixed structured meshes in terms of straightforward extensions of well-developed numerical schemes, application of fast solvers, absence of grid distortion, entanglement and massive re-gridding effects, and the ability to follow the evolution of interfaces through changes in topology without affecting the computational grid. There are of course some significant issues involved in making fixed grid methods work and these are also mentioned below.
2. Eulerian methods: In this class of methods, particularly for surfaces undergoing large deformations such as in free-surface flows or shattering of droplets, it is advantageous to dispense with tracking the interface as a curve or surface. Instead, in this class of methods the boundary is deduced from values on the mesh of a field variable which could be a volume-of-fluid (Hirt and Nichols, 1981, Brackbill et al., 1992, Kothe and Mjolsness, 1992, Scardovelli and Zaleski, 1999), a level-set (Osher and Sethian, 1988), or phase-field (Kobayashi, 1993, Wheeler et al., 1992), or the enthalpy in solidification problems (Voller and Prakash, 1987). The interface is then an isocontour of the appropriate field variable. Usually calculations are performed over a fixed Cartesian mesh. However, recently some Eulerian methods have been extended to curvilinear (Zhang et al.,

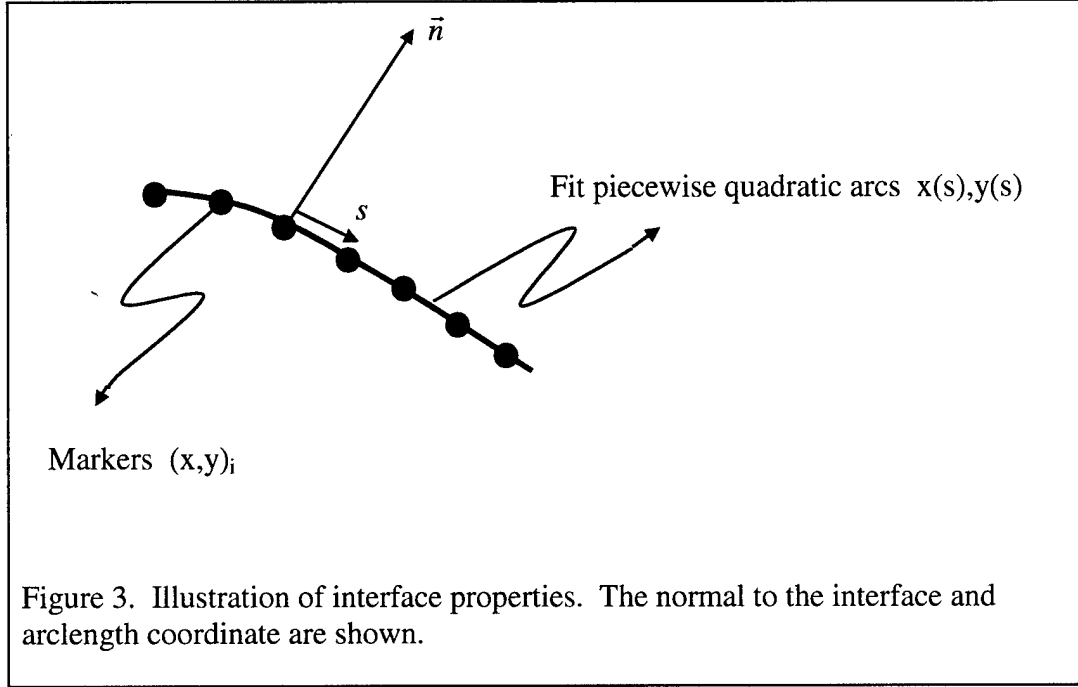
1998), adaptive (Sussman, 1997) and unstructured meshes (Barth and Sethian, 1998). Eulerian methods perform very well for a variety of moving boundary problems and are perhaps ideally suited to free-surface problems. However, in these problems, particularly when surface forces are to be included in the flow calculations, the interface essentially is diffuse and occupies a few grid cells in practical calculations. This may be undesirable in many problems both from an accuracy as well as physical reality/modeling standpoint. The problem treated in the current report is one example.

3. Mixed (Eulerian-Lagrangian) methods: This class of methods combines some advantages of the two approaches above. The interface is tracked explicitly as curves (or surfaces in 3D). The computations are performed on fixed meshes whose topology is independent of that of the interface. One example of this type of method is the immersed boundary technique used for a range of multifluid problems (Unverdi and Tryggvason, 1992, Juric and Tryggvason, 1996, Udaykumar et al., 1997) and for fluid-structure interaction problems in biofluids (Peskin, 1977, Fauci and Peskin, 1988). While explicitly tracking the interface, this method transmits the information regarding the discontinuity across the interface to the grid in much the same way as purely Eulerian methods, i.e. by casting the surface forces into a body force term in the governing equations. Therefore the solution reverts to a one-domain approach, i.e. the solver does not see a discontinuity at the location of the interface, but experiences distributed forces and material properties in the vicinity of the interface. As demonstrated by Beyer and Leveque (1992) this results in a method that is globally $O(h)$ accurate, where h is the grid spacing. On the other hand, the cut-cell treatment (Udaykumar and Shyy, 1995b, Udaykumar et al., 1996, Udaykumar et al., 1999, Ye et al., 1999) proceeds to reconstruct the domain on either side of the interface with attention to the immersed boundary and its geometry overlying the grid. Phases are treated separately and no smearing of the interface takes place at the formulation level. A conservative control volume treatment demanding care in assembly of fluxes is performed for cells on both sides of the interface. This method has been applied in recent work to problems involving immersed stationary and moving solid boundaries in incompressible flows where global second-order accuracy has been demonstrated.

The choice of moving boundary method from the general categories above depends to a large extent on its appropriateness for the physical problem chosen. In this report we demonstrate a fixed grid approach for high-speed impact that can be a powerful tool for numerical computation. The method presented in this report falls under the class of mixed methods. It operates on a fixed Cartesian mesh (the Eulerian part) while the interfaces move through the mesh (the Lagrangian part). The method treats the interfaces as discontinuities without smearing on the mesh, therefore it is a sharp interface method. The advantage of the fixed grid approach is obviously that grid topology remains simple while large distortions of the interface take place. The issues involved in explicit interface tracking are discussed below.

When interfaces are tracked explicitly, periodic reorganization of the interface information becomes necessary. This can result from dilation or compression of segments of the interface or due to topology changes of the interface. In 2D, mergers and breakups can be handled quite effectively (Udaykumar and Shyy 1995a, Juric and Tryggvason 1996). In 3D the operations can become more complicated (Snyder and Woodbury, 1993). Therefore, in 3D situations, explicit tracking of interfaces will be work-intensive in the context of mergers and breakups in comparison to purely Eulerian methods. However, there are physical problems for which explicit interface information becomes desirable; then interface tracking becomes the natural choice for immersed boundary treatment. One instance is when a solid-liquid boundary is being tracked and where the no-slip boundary condition is to be applied. This can be done for boundary-fitted grid computations quite naturally. For fixed grid computations also this can be done if the exact location of the interface, as provided by explicit tracking, is known (Udaykumar and Shyy 1997, Udaykumar et al. 1999, Ye et al. 1999). In fluid-structure interaction problems, such as in the dynamics of membranes (Dong et al., 1988, Kan et al., 1998), adhesion of cells to substrates in biofluids (Jones et al., 1995) or the dynamics of pliable aerodynamic surfaces (Shyy et al. 1996; Smith and Shyy, 1996; Fauci and Peskin, 1988), the forces generated within the membranes depend on the stretching and bending of the membranes. This requires information on the dilatation of the interface. Furthermore, for the case where the membrane is anchored to a surface as in the adhesion of a cell membrane to a substrate, the forces transmitted to the membrane need to be calculated (Dembo et al., 1988). Explicit tracking is ideally suited to these types of situations. The ability of mixed Eulerian-Lagrangian methods to incorporate both solid-liquid no-slip boundaries as well as fluid-fluid interfaces has been demonstrated in previous work by the authors (Udaykumar et al., 1997).

In the problem tackled in this report, an Eulerian-Lagrangian method can be used to good effect. Here we wish to simulate the interaction of a solid impactor with targets and to track the interface separating the two materials in time to determine the deformation of the two interacting bodies. When the materials are in contact following impact the material discontinuities at the interface need to be tracked without numerical diffusion. Explicit interface tracking is ideally suited to this task. Having chosen to explicitly track the boundaries, a fixed grid is used to compute the flow solutions in the presence of the moving boundaries. This allows an extension of highly accurate shock-capturing methods such as Essentially Non-Oscillatory or ENO (Harten et al., 1997, 1987, Shu and Osher, 1988, 1989) in the present case. These methods have been developed for scalar conservation laws in fixed grid settings to solve moving boundary problems with arbitrarily distorted interfaces. A Cartesian grid ENO formulation suffers little change when applied to the present problem. We now proceed to describe the method in detail.



5. Interface tracking algorithm

The interface is described by interfacial markers defined by the coordinates $X(s)$. The spacing between the markers is maintained at some fraction of the grid spacing, $0.5h < ds < 1.5h$. The convention adopted is that as one traverses the interface along the arclength, the material enclosed by the interface lies to the right. This is illustrated in Figure 3. The functions $x(s) = a_x s^2 + b_x s + c_x$ and $y(s) = a_y s^2 + b_y s + c_y$ are generated. The coefficients $a_{x/y}$, $b_{x/y}$ and $c_{x/y}$ at any interfacial point i are obtained by fitting polynomials through the coordinates (x_{i-1}, y_{i-1}) , (x_i, y_i) and (x_{i+1}, y_{i+1}) .

The coefficients $a_{x/y}$, $b_{x/y}$ and $c_{x/y}$ are stored for each marker point. The normal to the interface then points from the interior to the exterior of the object and is given by the equation:

$$\vec{n} = \left(\frac{-y_s}{\sqrt{x_s^2 + y_s^2}}, \frac{x_s}{\sqrt{x_s^2 + y_s^2}} \right) \quad (19)$$

The derivatives x_s , y_s are evaluated using central-differencing along the arclength coordinate s . Cubic splines were also tried without observable differences in the results for previous test problems. Therefore, central differencing was adopted since it is easily applicable to different end conditions for the boundaries.

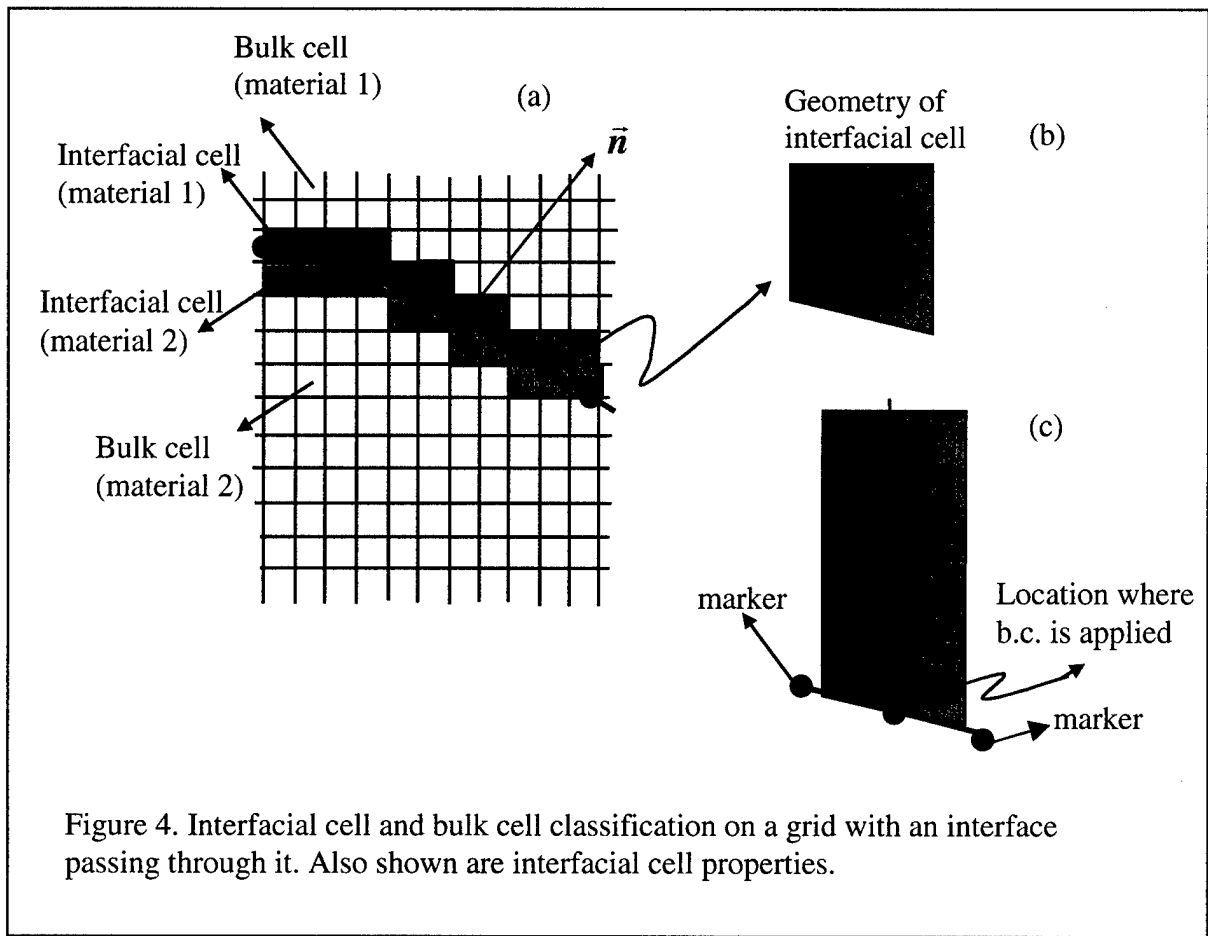


Figure 4. Interfacial cell and bulk cell classification on a grid with an interface passing through it. Also shown are interfacial cell properties.

6. Relationship between interface and grid

Once the interface has been defined, the information on its relationship with the grid has to be established. There may be several interfaces (henceforth called objects) immersed in the domain. Each of the objects may enclose material with different transport properties. Therefore it is necessary to identify which phase each computational point (i.e. cell center point) lies in. The procedure for obtaining this and related information has been discussed in detail in Udaykumar et al.(1999). The end result of the procedures are the following pieces of information which are required to set up the discretization scheme for the present method :

1. The interfacial cell in which each interface marker lies.
2. The interfacial marker which is closest in distance to a computational point.
3. The material in which each computational point in the mesh lies.
4. Several geometric details such as the shape of the resulting cut-cell, the locations where the interface cuts the cell faces and where it intersects the cell center lines (the dotted lines shown in Figure 4). These details of a cell are used in constructing the stencil for each interfacial cell.
5. A list of all interfacial cells.

These pieces of information regarding the interface and its relationship to the underlying grid are computed only in a lower-dimensional set of interface cells. Therefore using local searches and operations and data storage limited to this set of cells renders dealing with the interface and mesh relationship economical. In practical

runs the operations associated with obtaining the interface and mesh information is a small fraction of the computing time associated with field equation solver.

7. Numerical method for solving the field equations

Our interest in this work was to simulate the nonlinear wave propagation phenomena which occur in the high-speed impact of munitions on targets. Such problems involve highly dynamic, even discontinuous loading of the system. The waves generated upon the impact loading become propagating shock waves. Physically realistic weak solutions of the governing equations are therefore sought. There are a host of methods designed for the solution of hyperbolic conservation laws in the presence of shocks developed for high-speed aerodynamics applications (Leveque, 1990). The challenge in this report is to adapt these methods to compute wave propagation phenomena in solids where the constitutive relationship plays a role in the propagation of waves, and hence deformation of the media. We now present the local Lax-Friedrichs Essentially Non-Oscillatory (LLF-ENO) scheme used for solving the conservation laws. In order to apply this method for integration of the equations, it has to be established first that the system of equations under consideration is indeed hyperbolic, i.e. that the eigenvalues of the Jacobian matrix for the system are all real. This was verified to be the case for the range of physical parameters of interest (material properties, velocities etc.) in this work by Vanden (1998). For the homogeneous form of the 1D system written in conservative form, the eigenvalues are found to be:

$$\begin{aligned}\lambda_1 &= u \\ \lambda_2 &= u \\ \lambda_3 &= u \\ \lambda_4 &= u - \frac{\sqrt{\frac{\partial p}{\partial \rho} \rho^2 + \Gamma_0 \rho_0 (p - \rho u^2 + E)}}{\rho} \\ \lambda_5 &= u + \frac{\sqrt{\frac{\partial p}{\partial \rho} \rho^2 + \Gamma_0 \rho_0 (p - \rho u^2 + E)}}{\rho}\end{aligned}\tag{20}$$

These eigenvalues were found to be real for the range of parameters of interest in this work.

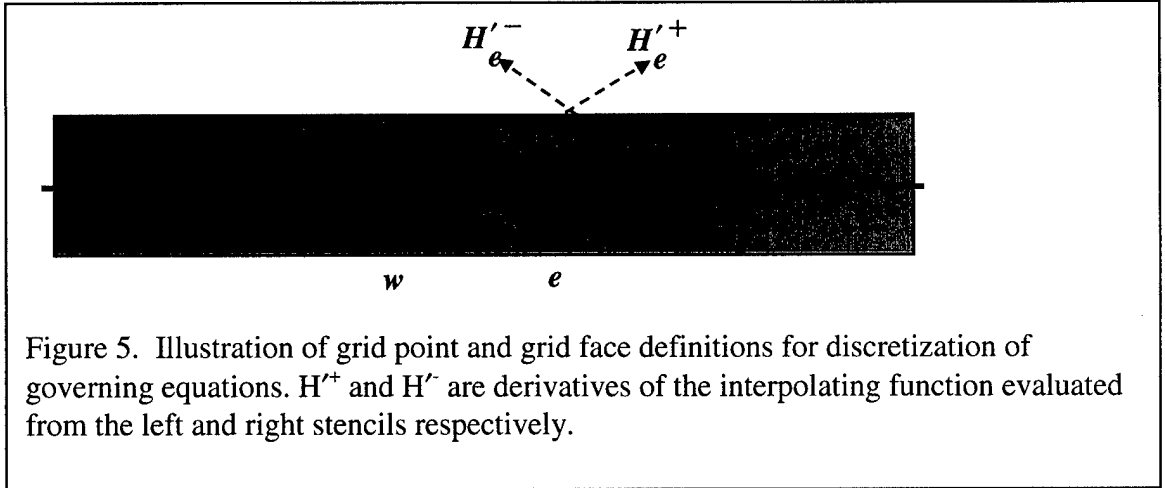
LLF-ENO discretization of the governing equations:

Consider the governing equation for one-dimensional transport:

$$\frac{\partial \bar{Q}}{\partial t} + \frac{\partial F(\bar{Q})}{\partial x} = S(\bar{Q})\tag{21}$$

Let

$$\frac{\partial \bar{Q}}{\partial t} = L(\bar{Q})\tag{22}$$



where

$$L(\bar{Q}) = -\frac{F_e - F_w}{x_e - x_w} + D(\bar{Q}) \quad (23)$$

F_e and F_w are the fluxes at the east and west faces shown, and x_e and x_w are the locations of the east and west faces respectively, as shown in Figure 5. D is an appropriate discrete operator for the source terms. In the current work, the source terms are discretized using a 2nd-order central difference scheme. This was found to be robust for the calculations performed. However, it may be necessary in future work to develop a more sophisticated differencing procedure for the source terms as well.

The three-step third-order in time Runge-Kutta scheme is used in this work and takes the form:

$$\begin{aligned} \bar{Q}^{(1)} &= \bar{Q}^{(n)} + \Delta t L(\bar{Q}^{(n)}) \\ \bar{Q}^{(2)} &= \frac{1}{4}(\bar{Q}^{(1)} + 3\bar{Q}^{(n)}) + \frac{1}{4}\Delta t L(\bar{Q}^{(1)}) \\ \bar{Q}^{(n+1)} &= \frac{1}{3}(2\bar{Q}^{(2)} + \bar{Q}^{(n)}) + \frac{2}{3}\Delta t L(\bar{Q}^{(2)}) \end{aligned} \quad (24)$$

The spatial order of accuracy of the ENO formulation used to solve Eq. (1) is determined by the interpolation practices used to evaluate the fluxes at the faces e and w , i.e. in obtaining F_e and F_w . A non-uniform mesh implementation of the fluxes in the ENO formulation is used here due to the presence of immersed boundaries, as illustrated in Figure 6. With particular reference to cell j , in the 1D case the interface can lie anywhere between x_j and x_{j+1} . The two materials are treated separately in the sharp interface formulation and the flux F_e is evaluated at a location $(x_j + x_{int})/2$. Thus, the spacing for cell j is different for the e and w faces. The flux evaluations for the ENO formulation comes from derivatives of an interpolating function $H(x)$ as follows:

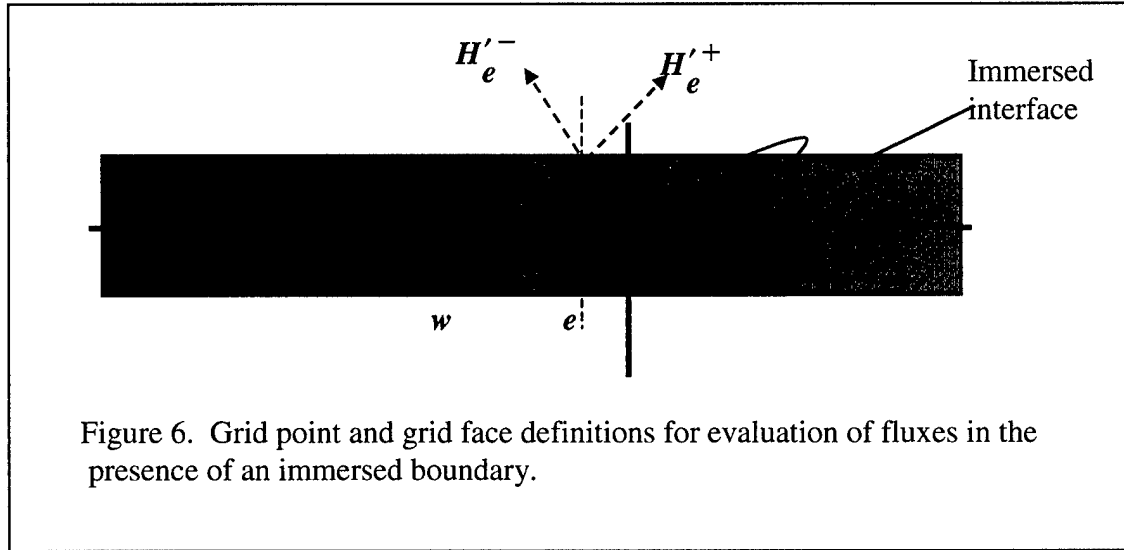


Figure 6. Grid point and grid face definitions for evaluation of fluxes in the presence of an immersed boundary.

$$F_e = \frac{d}{dx} [H(x)]_{x=x_e} \quad (25)$$

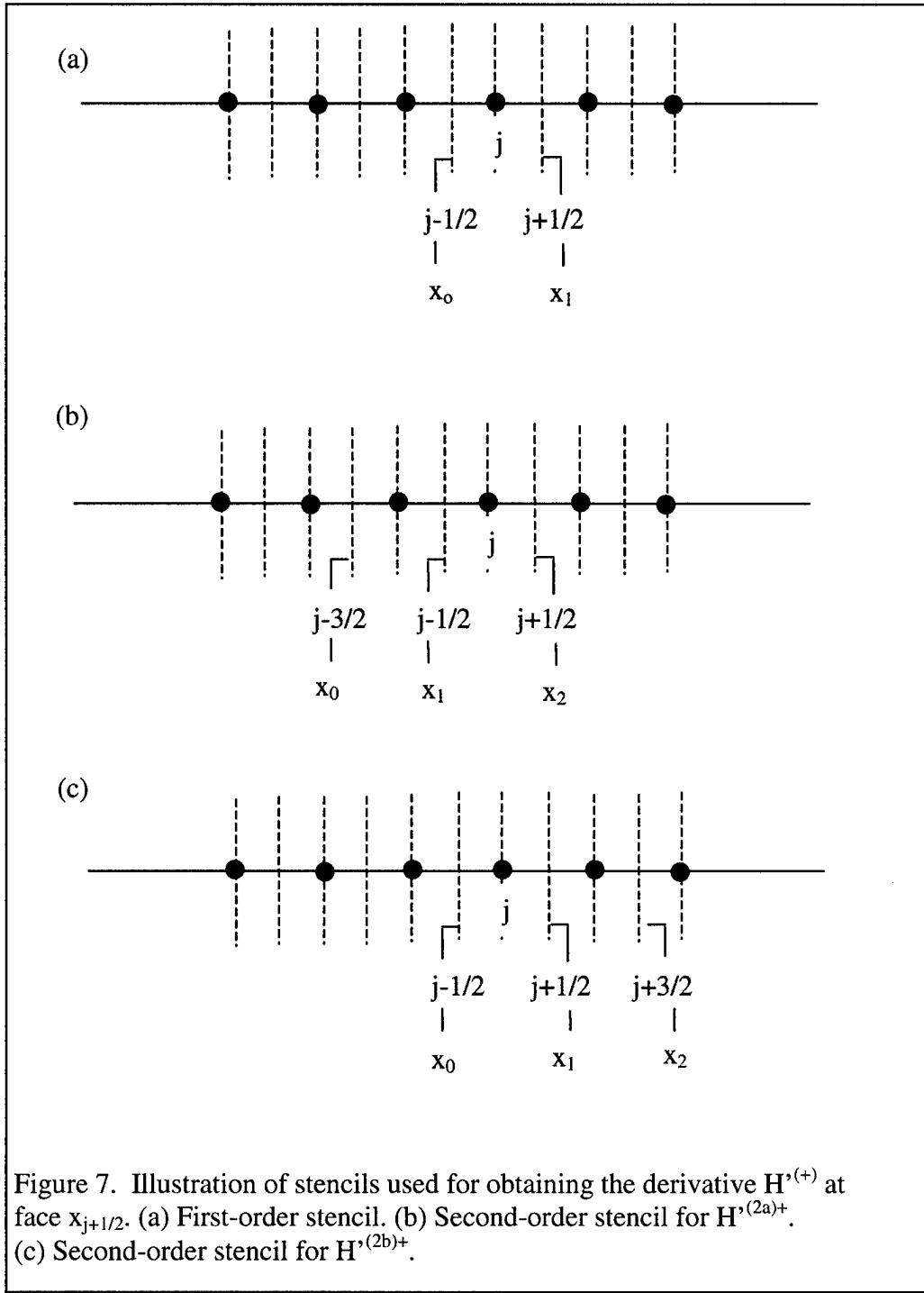
The derivatives are evaluated from divided differences and the flux evaluation is performed as follows:

$$F_e = F_e^+ + F_e^- = H'^+(x_e) + H'^-(x_w) \quad (26)$$

The superscripts (+) and (-) indicate the positive and negative direction fluxes at the face e under consideration as illustrated in Figure 5. The derivatives H' are obtained as explained below. Consider the interpolating function $H(x)$. In terms of the divided differences this function can be written as:

$$H(x) = H[x_0] + H[x_0, x_1](x - x_0) + H[x_0, x_1, x_2](x - x_0)(x - x_1) + O(h^3) \quad (27)$$

this interpolating polynomial can be carried to higher orders. We will restrict attention here to developing an $O(h^2)$ flux approximation. In the above $H[.,.]$ symbolizes the first divided difference and the higher-order divided differences are obtained successively. The Essentially Non Oscillatory (ENO) schemes (Shu and Osher, 1988,1989), are derived from a suitable choice of the stencil locations (x_0, x_1, x_2, \dots) from which the interpolating function is constructed.



For example, looking at Figure 7(a) it is clear that there is only one stencil possible for the first divided difference for control point location j , while there are two candidate stencils (shown in Figures 7(b) and (c)) for the second divided difference, as represented by the forward and backward differences in the divided difference table. The ENO scheme and its variants derive their essentially non-oscillatory property from the choice of stencils adopted. The original ENO scheme (Harten et al., 1987, Shu and Osher, 1988, 1989) chooses the “smoothest” stencil, i.e. the lesser of the two values for the divided differences obtained from the stencils in Figure 7(b) and (c). Weighted ENO schemes (Jiang and Shu, 1996) devise appropriate weights

for each candidate divided difference and then evaluate the weighted divided difference. The present formulation is based on the Convex ENO scheme proposed by Liu and Osher(1998) and chooses the divided difference value “closest” to the previous (here the first-) order flux chosen. It is this adaptive stencil choice procedure that enables the Lax-Friedrichs based ENO scheme to avoid smearing of solutions away from shocks while maintaining non-oscillatory character. Now the first divided difference is obtained as follows:

$$H'^+(x_e) = H^+ \left[x_{j-\frac{1}{2}}, x_e \right] = \frac{1}{2} (f(q[x_j]) + \alpha_{j+\frac{1}{2}} q[x_j]) \quad (28a)$$

and

$$H'^-(x_e) = H^- \left[x_e, x_{j+\frac{3}{2}} \right] = \frac{1}{2} (f(q[x_{j+1}]) - \alpha_{j+\frac{1}{2}} q[x_{j+1}]) \quad (28b)$$

Note that in general:

$$H^+[x_0, x_1]_{x=x_1} = \frac{1}{2} (f(q(\bar{x})) + \alpha(x_1)q(\bar{x})) \quad (29a)$$

$$H^-[x_0, x_1]_{x=x_0} = \frac{1}{2} (f(q(\bar{x})) - \alpha(x_0)q(\bar{x})) \quad (29b)$$

where

$$\bar{x} = \frac{(x_0 + x_1)}{2} \quad (30)$$

These of course apply to cells away from the immersed boundary such as cell $j+1$ in Figure 6. For cells that are adjacent to the immersed interface such as cell j in Figure 6, the flux evaluations need to be modified. Here, the east face is not the grid cell face but is located at $\frac{1}{2}(x_j + x_{int})$ where x_{int} is the location of the interface. Therefore, for cell j :

$$H'^+(x_e) = H \left[x_{j-\frac{1}{2}}, x_{int} \right] = \frac{1}{2} (f(q[x_j]) + \alpha_{j+\frac{1}{2}} q[x_j]) \quad (31a)$$

$$H'^-(x_e) = H \left[x_e, x_{int} \right] = \frac{1}{2} (f(q_{int}) - \alpha_{j+\frac{1}{2}} q_{int}) \quad (31b)$$

where q_{int} is the interfacial value of the convected scalar variable q . This value needs to be obtained from appropriate boundary conditions applied at the interface.

The first-order flux at the interface is then obtained using Eqs (26) and (28), or Equations (26) and (31) if cell j adjoins the interface. In order to determine the 2nd-order divided difference, the following steps are taken:

As a matter of notation we denote the first-order flux at cell face located at $x_{j+\frac{1}{2}}$ as :

$$\tilde{f}(j, j, +1) = H^+[x_{j-\frac{1}{2}}, x_{j+\frac{1}{2}}] = \frac{1}{2}(f(q(x_j)) + \alpha_{j+\frac{1}{2}} q[x_j]) \quad (32)$$

where the notation for the flux at the face in terms of $\tilde{f}(j1, j2, \pm 1)$ indicates that the flux is computed for the face of cell $j2$ using values at control point $j1$. The ± 1 indicates the direction of flux computed. Therefore, following this notation, the flux in the negative direction at cell face located at $x_{j+\frac{1}{2}}$ is given by:

$$\tilde{f}(j+1, j, -1) = H^-[x_{j+\frac{1}{2}}, x_{j+\frac{3}{2}}] = \frac{1}{2}(f(q(x_{j+1})) - \alpha_{j+\frac{1}{2}} q[x_{j+1}]) \quad (33)$$

The candidate second-order derivatives of the interpolating function $H(x)$ at cell face $x_{j+\frac{1}{2}}$ are:

$$\begin{aligned} H'^{(2a)+}(x_{j+\frac{1}{2}}) &= H^+[x_{j-\frac{3}{2}}, x_{j-\frac{1}{2}}] + \frac{(x_{j-\frac{3}{2}} + x_{j-\frac{1}{2}} - 2x_{j+\frac{1}{2}})}{(x_{j+\frac{1}{2}} - x_{j-\frac{3}{2}})} H^+[x_{j-\frac{3}{2}}, x_{j-\frac{1}{2}}] \\ &+ \frac{(2x_{j+\frac{1}{2}} - x_{j-\frac{3}{2}} - x_{j-\frac{1}{2}})}{(x_{j+\frac{1}{2}} - x_{j-\frac{3}{2}})} H^+[x_{j-\frac{1}{2}}, x_{j+\frac{1}{2}}] \end{aligned} \quad (34)$$

which can be written based on the notation in Eqs. (32) and (33) as :

$$H'^{(2a)+}(x_{j+\frac{1}{2}}) = \tilde{f}(j-1, j, +1) + A^{(2a)+} \tilde{f}(j-1, j, +1) + B^{(2a)+} \tilde{f}(j, j, +1) \quad (35)$$

where A and B are grid dependent factors determined by the locations of the stencil points chosen. Similarly, the other candidate second-order fluxes can be written as:

$$H'^{(2b)+}(x_{j+\frac{1}{2}}) = \tilde{f}(j, j, +1) + A^{(2b)+} \tilde{f}(j, j, +1) + B^{(2b)+} \tilde{f}(j+1, j, +1) \quad (36)$$

$$H'^{(2a)-}(x_{j+\frac{1}{2}}) = \tilde{f}(j, j, -1) + A^{(2a)-} \tilde{f}(j, j, -1) + B^{(2a)-} \tilde{f}(j+1, j, -1) \quad (37)$$

$$H'^{(2b)-}(x_{j+\frac{1}{2}}) = \tilde{f}(j+1, j, -1) + A^{(2b)-} \tilde{f}(j+1, j, -1) + B^{(2b)-} \tilde{f}(j+2, j, -1) \quad (38)$$

Similar expressions for the 3rd- and higher-order derivatives can be obtained. Therefore, for the second-order fluxes at the face $j+1/2$ there are two candidates each for the (+) and (-) direction contributions.

In the presence of immersed boundaries the discretization in the cells adjoining the interface only will need to be modified in two ways:

1. The interface boundary conditions will appear in the flux contributions from the interface side as in Eq. (31).
2. The stencil choices possible at such cells will be limited in the direction in which the interface lies. For example, with reference to Figure 6, for cell j there will be one first-order stencil in each direction as for the interior cells. However, for interfacial cell $j+1$, there can be only one choice of second order flux for the estimation of $H^{(-)}$.

These considerations are no different in fact from that at the cell immediately in the interior of the domain boundary. Therefore the immersed boundary treatment for evaluating fluxes is no different from that for domain boundary cells. Apart from these considerations the fluxes for the cell j adjoining the immersed boundary are constructed using Eq (31) except that the values of q_{int} , i.e. boundary conditions on the immersed interface need to be used instead of the grid point q_j values in the Eq. (28). It is not readily apparent how to compute the boundary values for all the dependent variables in the particular physical problem being computed. Some physically based boundary conditions can be imposed based on the physics of the impact phenomena. However, some of the physical quantities will require numerical boundary conditions as in other systems of PDEs. The boundary conditions chosen and the rationale for the choice are explained in the following sections.

8. Boundary and interface conditions in the 1D case

If the rods are semi-infinite the boundary conditions at $x=0$ and $x=L$ (L being the extent of the domain along the x -axis) correspond to open boundary conditions (i.e. zero-gradient conditions). However, for finite size rods lying within the domain as shown in Figure 1, two types of boundary conditions need to be considered.

Type 1: Material-material (M-M) boundary condition:

The interface between the two rods at the point of impact is one separating two materials. When the two materials are in contact continuity dictates that the material point velocities at the interface are equal, the total stresses are equal and the temperatures are equal. Therefore:

$$u^+ = u^- = u_{int} \quad (39)$$

$$\sigma_x^+ = \sigma_x^- = \sigma_{int} \quad (40)$$

$$T^+ = T^- = T_{int} \quad (41)$$

However, there are six dependent variables $(\rho, u, p, E, s_x(\sigma_x), \bar{\epsilon})$ in the governing equations for the 1D system. The physically available boundary conditions and the eos yield only four conditions on these variables. Therefore one needs to devise numerical b.c.s for the remaining variables. Several alternative formulations of b.c.s were tried. Some of these yielded unphysical solutions. The viable set of b.c.s determined from numerical experiments are as follows:

$$\rho^\pm = \Xi(\rho_j) \quad (42)$$

$$E^\pm = \Xi(E_j) \quad (43)$$

$$\bar{\epsilon}^\pm = \Xi(\bar{\epsilon}_j) \quad (44)$$

$$u^\pm = I(u_j) \quad (45)$$

$$p^\pm = eos(\rho^\pm, (\rho u^2)^\pm, E^\pm) \quad (46)$$

$$(s_x + p)^\pm = I((s_x + p)_j) \quad (47)$$

Here Ξ is an appropriate extrapolation operator. The choice of the operator determines the order of accuracy of the numerical b.c. at the interface. We perform linear extrapolation of variables from the suitably chosen grid point values (e.g. $j+1$ and $j+2$ on the (+) and $j-1$ and j on the (-) side of the interface in Figure (6) to the interface. Here I is an interpolation operator. Since the velocity is continuous across the interface the value at the interface, according to Eq. (39) can be obtained by interpolating from the grid points straddling the interface. Again the order of interpolating operator determines the accuracy of the interface b.c. In our case I is a distance-weighted linear interpolant.

Type 2: Material-void (M-V) boundary condition:

Before the rods impact there is a void separating them. Also, if the rods are finite the material at the grid points to the right of the right rod and left of the left rod are void regions. Therefore the ends of the rods are material-void interfaces. Again, the physics dictates the following b.c.s on the material-void interface:

$$\sigma_x = \sigma^+ = \sigma^- = 0 \quad (48)$$

along with the equation of state which applies in the material at the interface. This again requires imposition of numerical boundary conditions at such interfaces for the remaining variables. The appropriate numerical b.c.s were found to be:

$$\rho^- = \Xi(\rho_j) \quad (49)$$

$$E^- = \Xi(E_j) \quad (50)$$

$$\bar{\epsilon}^- = \Xi(\bar{\epsilon}_j) \quad (51)$$

$$u^- = \Xi(u_j) \quad (52)$$

$$p^- = eos(\rho^-, (\rho u^2)^-, E^-) \quad (53)$$

$$(s_x + p)^- = 0 \quad (54)$$

Note that within the current Eulerian-Lagrangian framework, the boundary conditions are applied and the discretization is performed in a one-sided manner, i.e., the information for each material is drawn from within that material. Therefore, at the material-material boundary the boundary conditions need to be determined on both the (+) and (-) sides of the interface and stored. The discretization at point j in Figure (6) therefore uses the values on the (-) side of the interface while that at point $j+1$ uses the values on the (+) side of the interface. Finally, once the interface velocity is obtained from the above boundary conditions, the interface position is updated explicitly as:

$$x_{\text{int}}^{(n+1)} = x_{\text{int}}^{(n)} + \delta t u_{\text{int}}^{(n)} \quad (55)$$

9. 1D Results

The 1D system for which computations were performed is shown in Figure 1. Since the results presented below are for the case of uniaxial strain, the two materials in impact are termed plates. The plates were initially placed in contact at the midpoint of the domain and given initial velocities which caused the impact and the interface separating the two materials then traveled over the fixed grid. The position of both the interface separating the two materials as well as the ends of the rods (in the case of finite rods) were tracked over the grid. Thus the positions of the plate end points are tracked explicitly.

Results of three cases are shown in the following for the 1D case. These involve the traversal of plate end points of the material-material and material-void interfaces on the fixed mesh. All computations are performed using the material properties for Copper. The values used were a shear modulus of $G=4.5 \times 10^{10}$ Pa, density $\rho_0=8.93 \times 10^3$ kg/m³, and an idealized stress-strain relationship giving the equivalent stress:

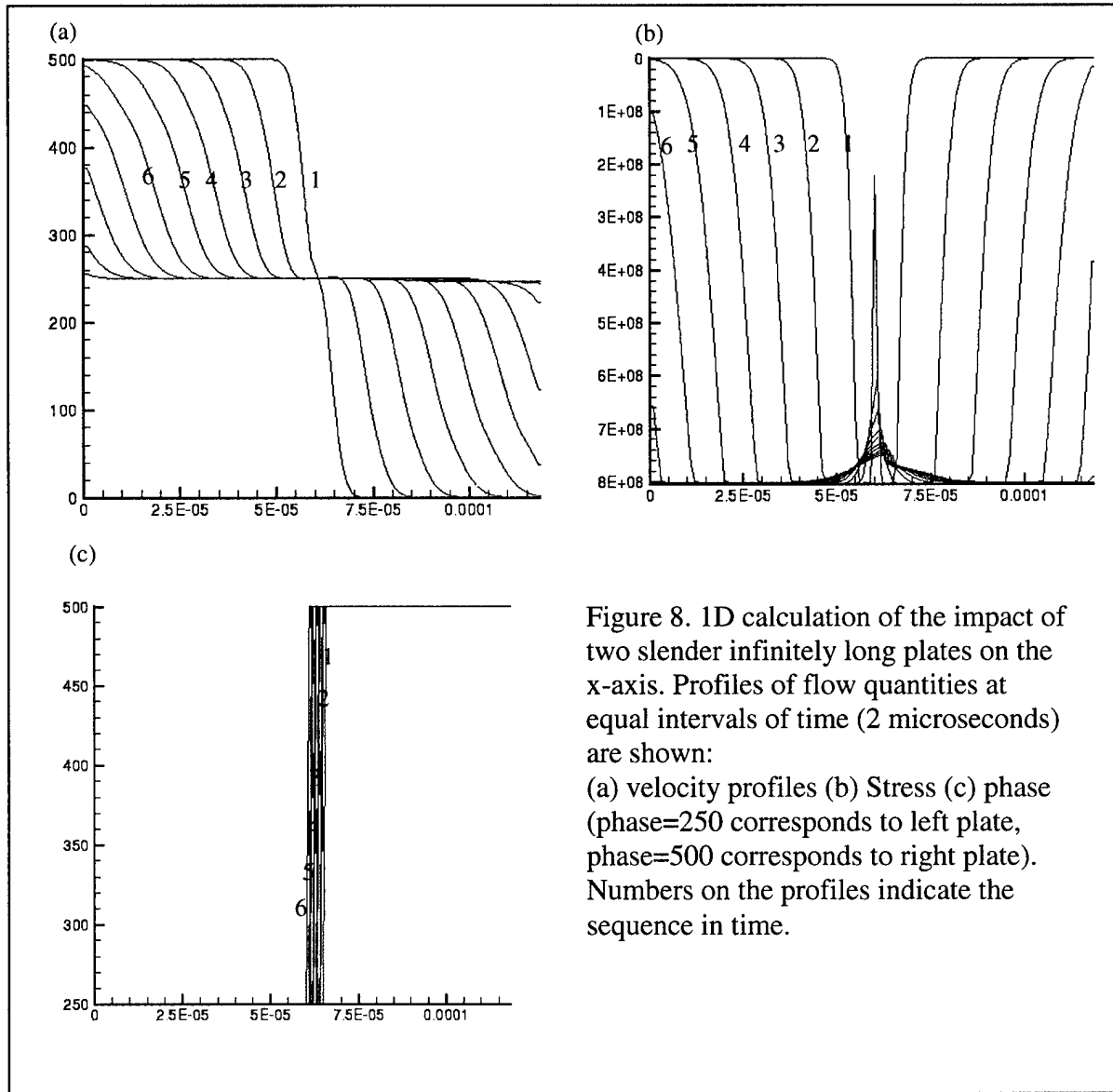
$$\sigma_e = \sqrt{\frac{3}{2} s_{ij} s_{ij}} = H(\bar{\epsilon}) = H_0 + H' \bar{\epsilon} \quad (56)$$

where $H_0=1.20 \times 10^9$ Pa and a constant $H' = 0.12 \times 10^9$ Pa. Also in the Mie-Gruneisen equation of state for copper, $\Gamma_0=2$, $c_0=3.94 \times 10^3$ m/s and $s=1.49$.

The mesh used in each case consists of 100 points in the domain. There are four interfacial points tracked on the mesh corresponding to the ends of the two bars. The computations are carried to significant times after impact so that the interfaces move over several mesh cells.

In Figure 8, we show the case of impact of two plates of semi-infinite extent. The plates are initially positioned such that impact takes place at $x = 0.6 \times 10^{-5}$, the center of the domain. The left plate has a velocity before impact of 500 m/s. The interface points (plate end points) at the center in the domain are supplied with the material-material boundary conditions on the (+) and (-) sides. At the left and right end of the domain, zero-gradient conditions are applied for all quantities since the plate is assumed to be semi-infinite. In each figure we show the profile along x of the flow variables at equal intervals of time ($\Delta t = 2$ microseconds) after impact. In figure 8(a) the velocity profiles are shown. In Figure 8(c) we show the phases at each point in the grid, again at equal time intervals of 2 microseconds. It can be seen that the interface travels to the right due to the impact. In Figure 8(b) the profiles of the equivalent stress show the large gradients developed at the interface following impact. The resulting wave propagation phenomena lead to the propagation of stress waves and corresponding strains through the plates. Symmetry about the point of impact is maintained during the computation as it should be. At the material-material interface point the material-material boundary conditions discussed above have been used. Clearly, in the presence of the moving material-material boundary, the solution of the governing equations leads to a stable physical solution.

In Figure 9 we show the solutions for the case where there are two finite plates in the domain. The left plate initially has a velocity to the right of 500 m/s. The right plate is initially stationary. The finite plates initially occupy the regions $1 \times 10^{-5} < x_l < 3 \times 10^{-5}$ for the left plate and $3 \times 10^{-5} < x_r < 5 \times 10^{-5}$ for the right plate. We show the profiles for velocity (Figure 9(a)), equivalent stress (Figure 9(b)), and phases (Figure 9(c)) in the domain at equal intervals of time of $\Delta t = 2$ microseconds. In this case, while the waves propagate in the two plates, the plates are physically moving and deforming over the mesh. The gradual equalization of the velocities of the material points in the two plates is seen in Figure 9(a). As the computation proceeds the maximum material point velocity oscillates between the two plates. As can be seen in the profile 7 in Figure 9(a), the particle velocity in each plate is tending to the mean value of 250 m/s. Immediately after impact we see very large stresses developing at the point of impact. As can be seen in Figure 9(c) the two plates are moving to the right and the four interfaces, namely the material-material and material-void interfaces are tracked through the mesh.



In Figure 10, we compute the case of two finite plates impacting with opposite velocities. Initially the plates occupied the regions, $1 \times 10^{-5} < x_l < 6 \times 10^{-5}$, and $6 \times 10^{-5} < x_r < 1.1 \times 10^{-5}$. The left plate was given a velocity of 250m/s and the right plate of -250 m/s. Note in this case the final velocities by symmetry should tend to cancel, and both plates should be stationary on the x-axis, i.e. one expects that the wave propagation and reflection from the material-void interfaces at the far ends of the plate should take place symmetrically. Clearly, this symmetry is well maintained by the computations. Initially, as seen in Figure 10(b) large gradients in stress are initially developed in the region close to impact. The longitudinal oscillation of the plates about the mean position can be seen from the profiles in Figure 10.

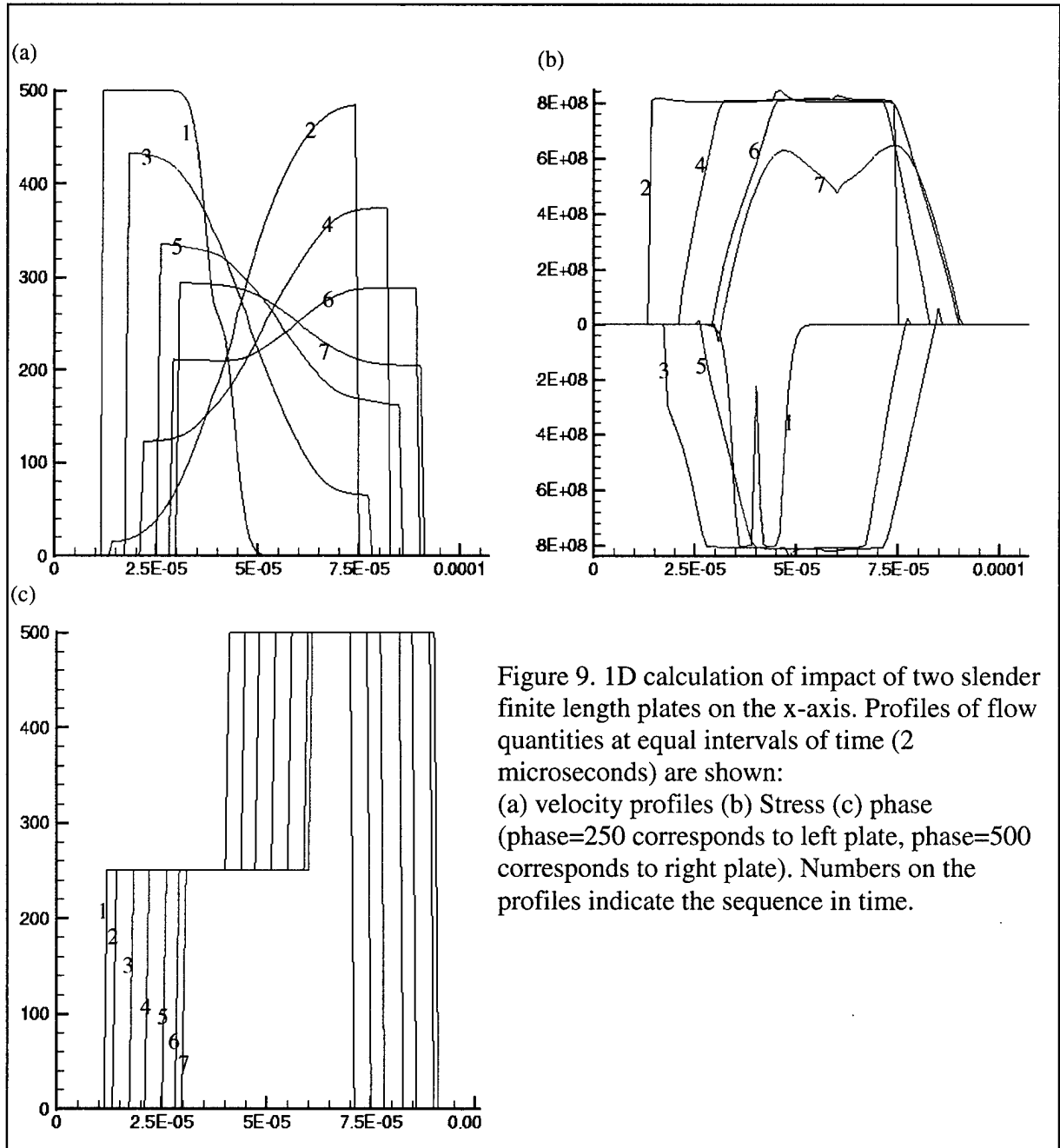
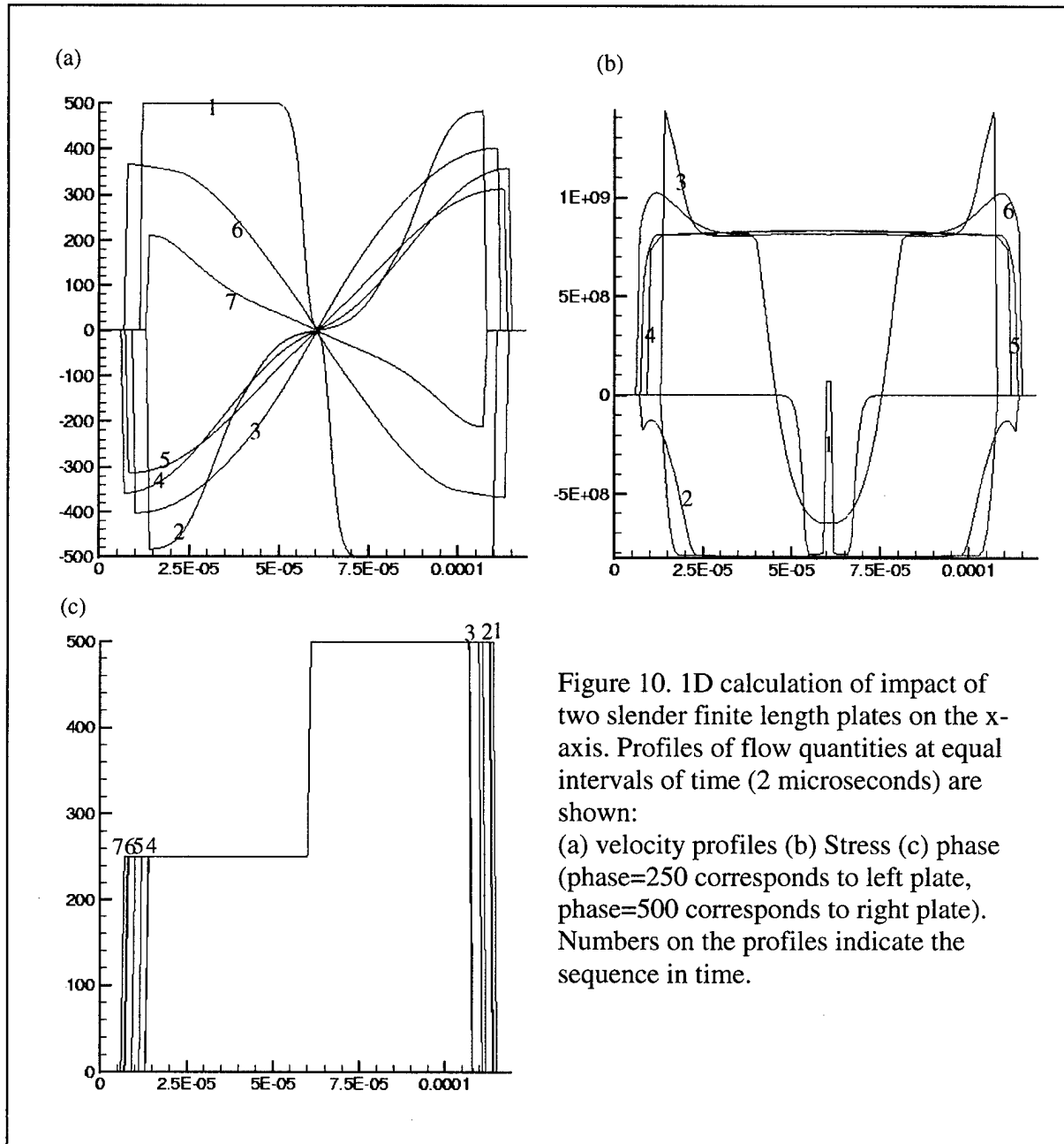


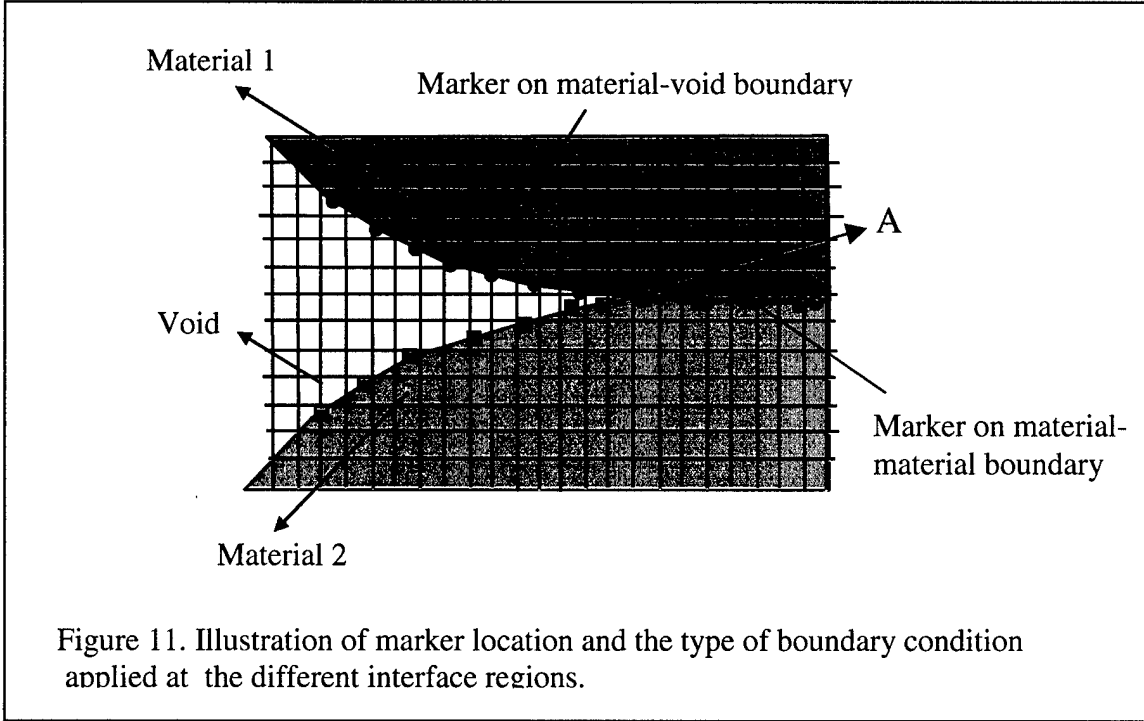
Figure 9. 1D calculation of impact of two slender finite length plates on the x-axis. Profiles of flow quantities at equal intervals of time (2 microseconds) are shown: (a) velocity profiles (b) Stress (c) phase (phase=250 corresponds to left plate, phase=500 corresponds to right plate). Numbers on the profiles indicate the sequence in time.

10. Boundary and initial conditions in the 2D case

A schematic for the interface treatment in 2D computations is shown in Figure 11. The impactor and target are initially placed some distance apart and impact is initiated by giving a uniform velocity to the impactor while the target remains stationary. Therefore, initially only particle velocities and other material properties such as density have non-zero values, while stresses are set to zero. In the 2D case the boundary conditions are based on the physically imposed ones and numerical b.c.s obtained based on the experience gained from the 1D situation and tested by numerical experiments. In contrast with the 1D case however, in 2D some regions of



the interface can be in material-material contact and others can be exposed to a void. This is illustrated in Figure 11. Here the region of contact between two curved boundaries in collision is shown. The individual marker points which define the two interfaces are also shown in the Figure 11. Interfacial boundary conditions are applied at these marker locations on the interface. Therefore, as can be seen in the figure, an interfacial marker in the material-material region can have an immediate neighbour in the material-void region of the interface. Therefore, at each instant of the interface deformation the interface markers have to be classified as material-material or material-void markers and the appropriate b.c.s obtained. Thus two immediately



adjacent interfacial marker neighbours can have entirely different b.c.s imposed on them.

Type 1: Material-material interface

Boundary conditions in the material-material case are developed based on the physically required conditions of equal material point velocities at the interface for the two materials, and the continuity of stress and temperature. These conditions can be stated as:

$$u^+ = u^- = u_{\text{int}} \quad (57)$$

$$v^+ = v^- = v_{\text{int}} \quad (58)$$

$$\sigma_{xx}^+ = \sigma_{xx}^- = (\sigma_{xx})_{\text{int}} \quad (59)$$

$$\sigma_{yy}^+ = \sigma_{yy}^- = (\sigma_{yy})_{\text{int}} \quad (60)$$

$$\sigma_{xy}^+ = \sigma_{xy}^- = (\sigma_{xy})_{\text{int}} \quad (61)$$

$$T^+ = T^- = T_{\text{int}} \quad (62)$$

Along with the eos for the pressure these constitute 7 physically imposed conditions at the interface for the nine independent variables $(\rho, u, v, p, E, s_{xx}, s_{yy}, s_{xy}, \bar{\epsilon})$. This necessitates numerical boundary conditions to be developed for the remaining dependent variables. We obtain these based on extensions of the 1D boundary conditions and verify that they provide numerically stable, convergent solutions

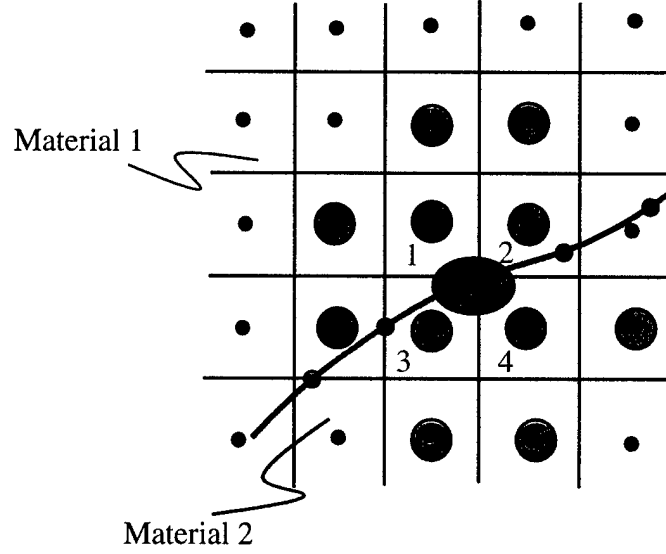


Figure 12. Illustration of marker and grid points involved in applying the material-material boundary condition.

without unphysical behaviors such as overshoots or oscillations. The numerical implementation of the boundary conditions can be explained with reference to Figures (12) and (13).

For the material-material contact situation shown in Figure 12, the boundary conditions are imposed on the interfacial markers shown on the interface by the filled circles. The viable boundary conditions are determined to be:

$$\rho^{\pm} = \Xi(\rho_{i,j}) \quad (63)$$

$$E^{\pm} = \Xi(E_{i,j}) \quad (64)$$

$$\bar{\epsilon}^{\pm} = \Xi(\bar{\epsilon}_{i,j}) \quad (65)$$

$$p^{\pm} = eos(\rho^{\pm}, (\rho u^2)^{\pm}, (\rho v^2)^{\pm}, E^{\pm}) \quad (66)$$

$$u^{\pm} = I(u_{i,j}) \quad (67)$$

$$v^{\pm} = I(v_{i,j}) \quad (68)$$

$$(s_{xx} + p)^{\pm} = I((s_{xx} + p)_{j,j}) \quad (69)$$

$$(s_{yy} + p)^{\pm} = I((s_{yy} + p)_{j,j}) \quad (70)$$

$$(s_{xy})^{\pm} = I((s_{xy})_{j,j}) \quad (71)$$

In the above the operators Ξ and I are the extrapolation and interpolation operators respectively. The subscripts (i,j) indicate values on the grid while superscripts \pm

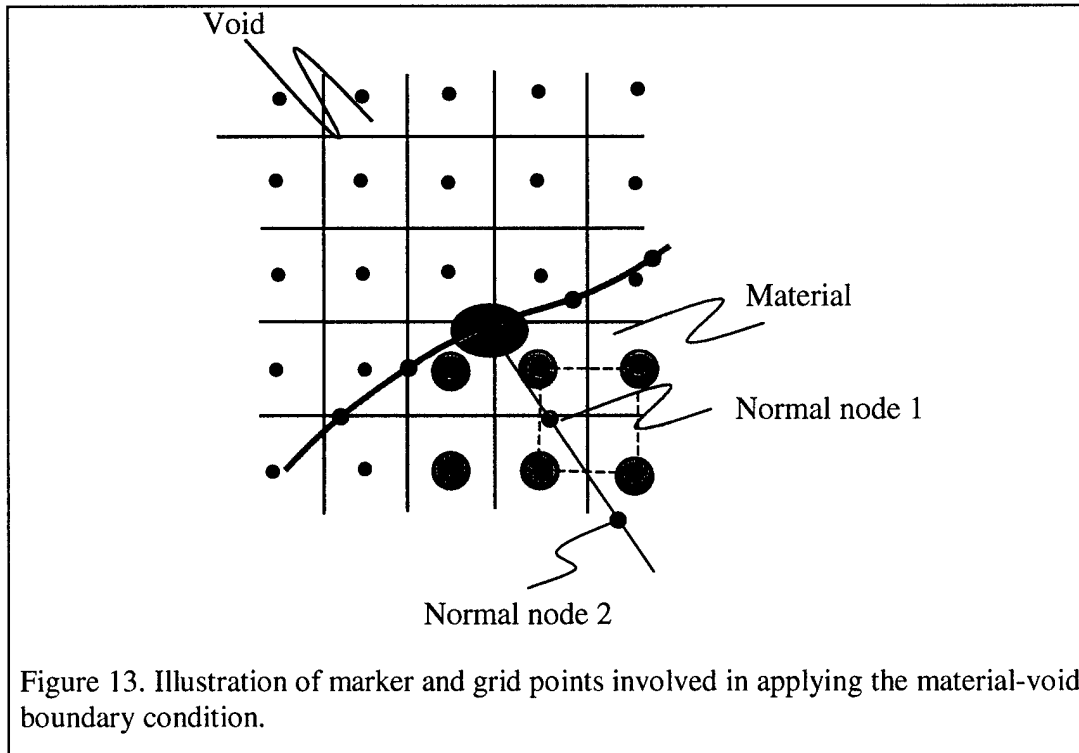


Figure 13. Illustration of marker and grid points involved in applying the material-void boundary condition.

indicate values on the (+) and (-) sides of the interface. In particular for the interfacial marker indicated by the ellipse in Figure 12, a bilinear interpolation operator is used to estimate the variables which are continuous across the interface. The points 1,2,3 and 4 straddle the interface marker in question and bilinear interpolation is performed based on the location of the interface marker and the location of these grid points. Note that on a Cartesian mesh, having obtained the information regarding the interface and its relation to the mesh as discussed in Section 6, it is a simple matter to choose the points in the bilinear interpolant. The extrapolation operator used for obtaining the values of variables not governed by continuity conditions is somewhat less straightforward in 2D. For example, with particular reference to the interfacial marker in focus in Figure 13 (in the ellipse), extrapolation has to be performed from values at grid points within the interior of the material. In order to do so, a normal is extended from the interfacial marker in question into the material. The values at two nodes on the normal placed a distance h (the grid spacing) apart are obtained by bilinear interpolation from grid points straddling each normal node point. For normal node point 1 for example, the values are interpolated from grid points connected by dashed lines. The value at the interface is then obtained by extrapolating from the values at the two nodes along the extended normal to the interface.

Type 2: Material-void interface

For a material-void interface, the physically imposed conditions on the interface are that the traction be zero. In the present case we let the stresses vanish on the free surface as:

$$\sigma_{xx}^+ = 0 \quad (72)$$

$$\sigma_{yy}^+ = 0 \quad (73)$$

$$\sigma_{xy}^+ = 0 \quad (74)$$

Along with the eos for pressure, which applies at the interface on the material side, the imposed b.c.s account for only four of the nine independent variables. Therefore numerical b.c.s are required at the interface and these are devised based on extensions from the 1D case and by experimentation such that the b.c.s imposed do not lead to development of unphysical features in the flowfield. The b.c.s imposed on the material side of the interface are as follows:

$$\rho^- = \Xi(\rho_{i,j}) \quad (75)$$

$$E^- = \Xi(E_{i,j}) \quad (76)$$

$$\bar{\epsilon}^- = \Xi(\bar{\epsilon}_{i,j}) \quad (77)$$

$$u^- = \Xi(u_{i,j}) \quad (78)$$

$$v^- = \Xi(v_{i,j}) \quad (79)$$

$$p^- = eos(\rho^-, (\rho u^2)^-, (\rho v^2)^-, E^-) \quad (80)$$

$$(s_{xx} + p)^- = 0 \quad (81)$$

$$(s_{yy} + p)^- = 0 \quad (82)$$

$$(s_{xy})^- = 0 \quad (83)$$

Note that no b.c.s are required on the void side of the interface.

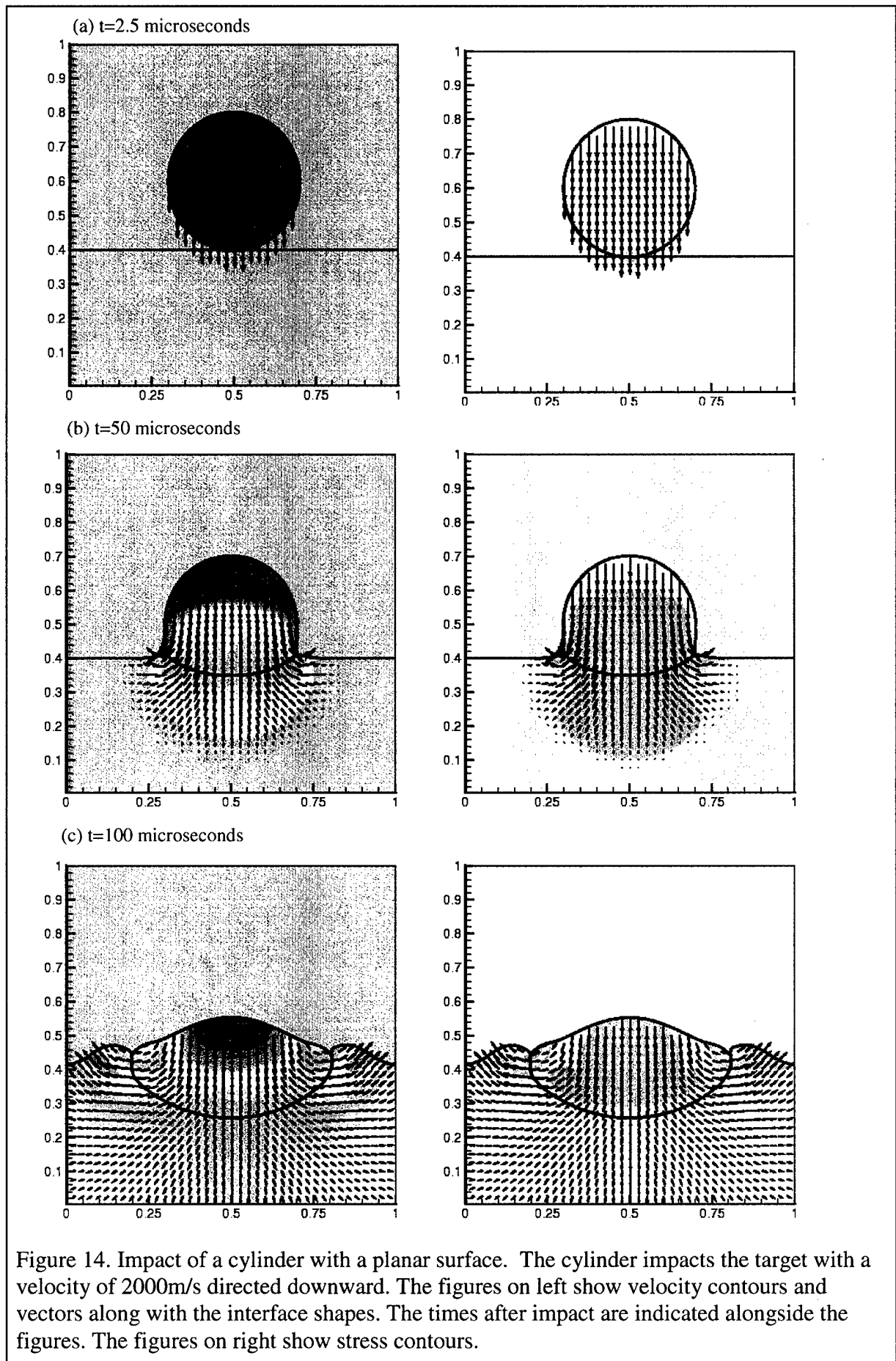
11. Results of 2D computations

2D computations were performed in a square domain of size 1m x 1m as illustrated in Figure 2. As shown there the objects were placed some distance apart on the mesh and impact was initiated by prescribing a velocity to one or both interfaces. Initially there is a region of void between the two interfaces. When the interface markers lie in a material-void region of the interface we apply the boundary conditions of type 2 (M-V) on such markers. On markers in the material-material regions of the interface, b.c.s of type 1 (M-M) are applied. Note that the discretization procedure in 2D requires the value of q_{int} at interface location not coincident with the interfacial markers. To obtain the interfacial value of flow quantities at such points, we interpolate along the interface using a linear function fit between successive markers straddling the point as shown in Figure 4(c). Higher-order interpolation along the interface is of course possible but was found to lead to erroneous behaviour due to the large gradients along the interface at regions where there is an abrupt switch from a M-M to M-V type boundary condition. This implies that at points where the interfaces go from being in the material-material contact

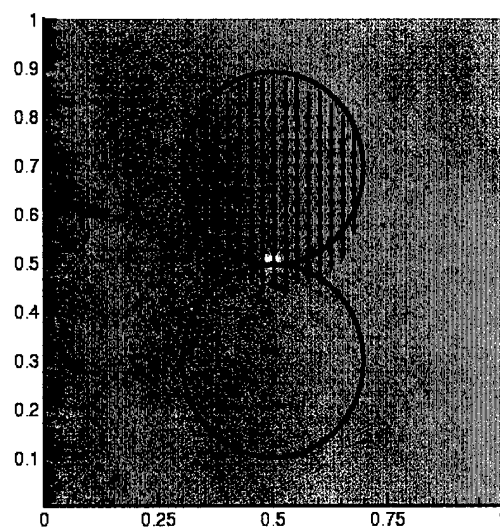
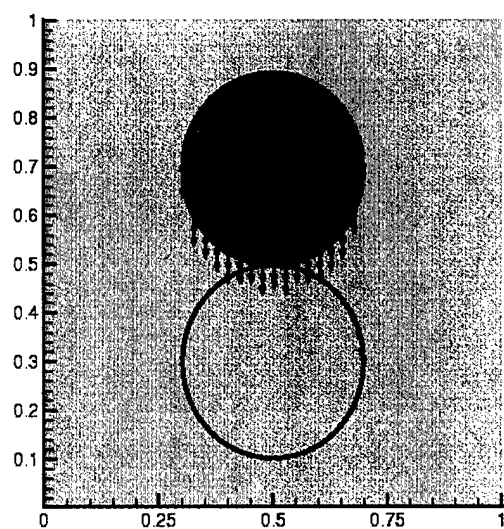
situation to material-void situation, such as point A in figure 11, we introduce a lower-order interpolation practice to avoid overshoots.

We have tried several challenging cases for the evolution of the interfaces after impact. In the first case, presented in Figure 14, we show the impact of a copper cylinder with a copper planar surface. Both surfaces are copper and the material properties in the model correspond to that metal. In the figure, we show on the left the contours of particle velocity magnitude in the impactor and the target along with the velocity vectors in the flow domain. On the right we show contours of equivalent stress. Also shown in each of the figures is the shape of the boundaries of the two materials. As can be seen in these figures there is an abrupt transition in the corners from a material-material interface to a material-void interface for each material. Appropriate boundary conditions as discussed in Section 10 are applied in these regions. Zero-gradient conditions are applied at the sides of the domain assuming that the target has infinite extent in all except the +y direction. Figures 14(a), (b) and (c) correspond to time instants $2.5 \mu\text{s}$, $50 \mu\text{s}$ and $100 \mu\text{s}$ after impact respectively. The progression of the elastic-plastic waves and the formation of large gradients in the velocity as well stress fields is evident from the figure. At the rim of the impactor, the interfaces are constantly in collision since the material-void interfaces are being pushed against each other to form material-material interfaces. Therefore the rim of the impact region registers large stress and correspondingly, strain values. Stress waves are propagated into the materials from this point. In Figure 14(c) it can be seen that the velocity field is such as to continuously push the impactor into the target leading to the production of an upswell in the target material around the rim. This is also indicated clearly by the velocity vectors shown. Regions of compression and tension are seen from the contours of stress. The computational time for a 100×100 mesh calculation to the stage shown in Figure 14(c) is about one hour on a DEC-Alpha 5000 computer. No attempt has been made to optimize the code and it should be possible to decrease computational times significantly.

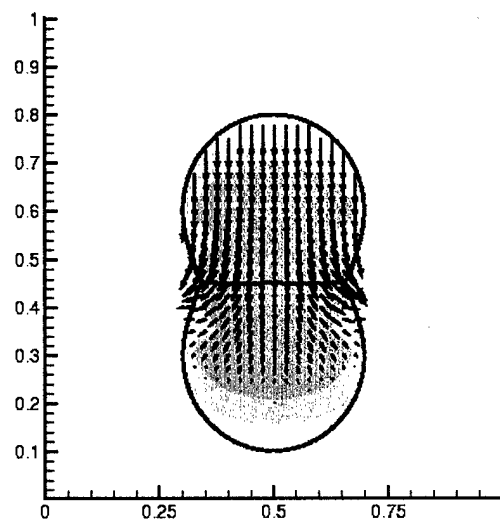
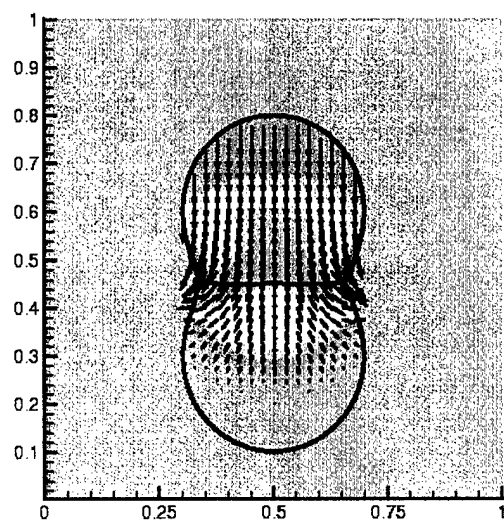
The next case corresponds to the impact of two cylindrical objects. Initially the lower object is stationary and the upper object is placed some distance away. The upper object then is projected with a velocity of -2000 m/s and impact with the lower object results in the situation shown in the figure. Figures 15(a), (b), (c) and (d) correspond to $2.5 \mu\text{s}$, $50 \mu\text{s}$, $100 \mu\text{s}$ and $150 \mu\text{s}$ after impact respectively. The lower object acquires velocity after impact and is allowed to move freely downward through the mesh as the velocity field develops. The velocity vectors show that the impact causes a flattening of the interfaces and that the lower target deforms symmetrically with respect to the impactor. Again the rim of the impact region shows large stress concentrations due to the continuous compression of the interfaces at that point by incorporation of the material-void interfaces.



(a) $t=2.5$ microseconds



(b) $t=50$ microseconds



(c) $t=100$ microseconds

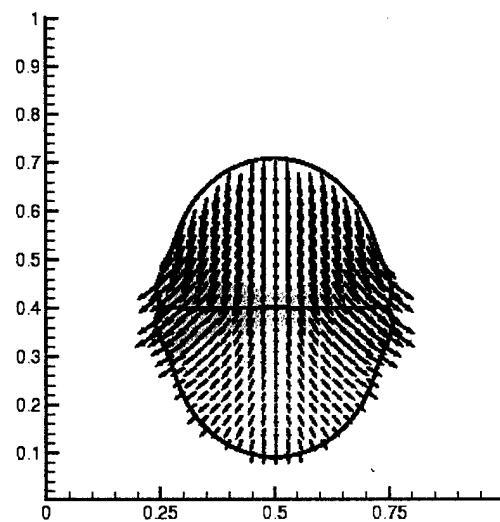
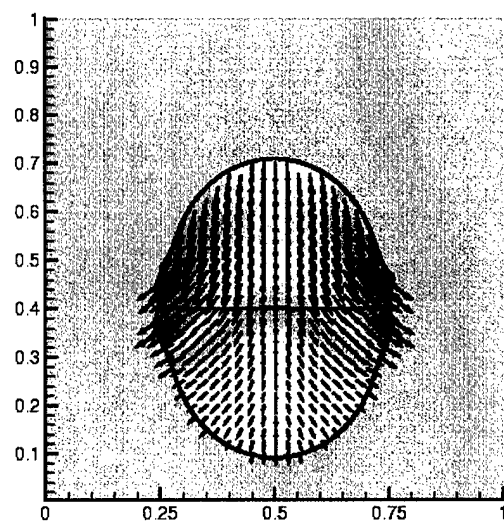
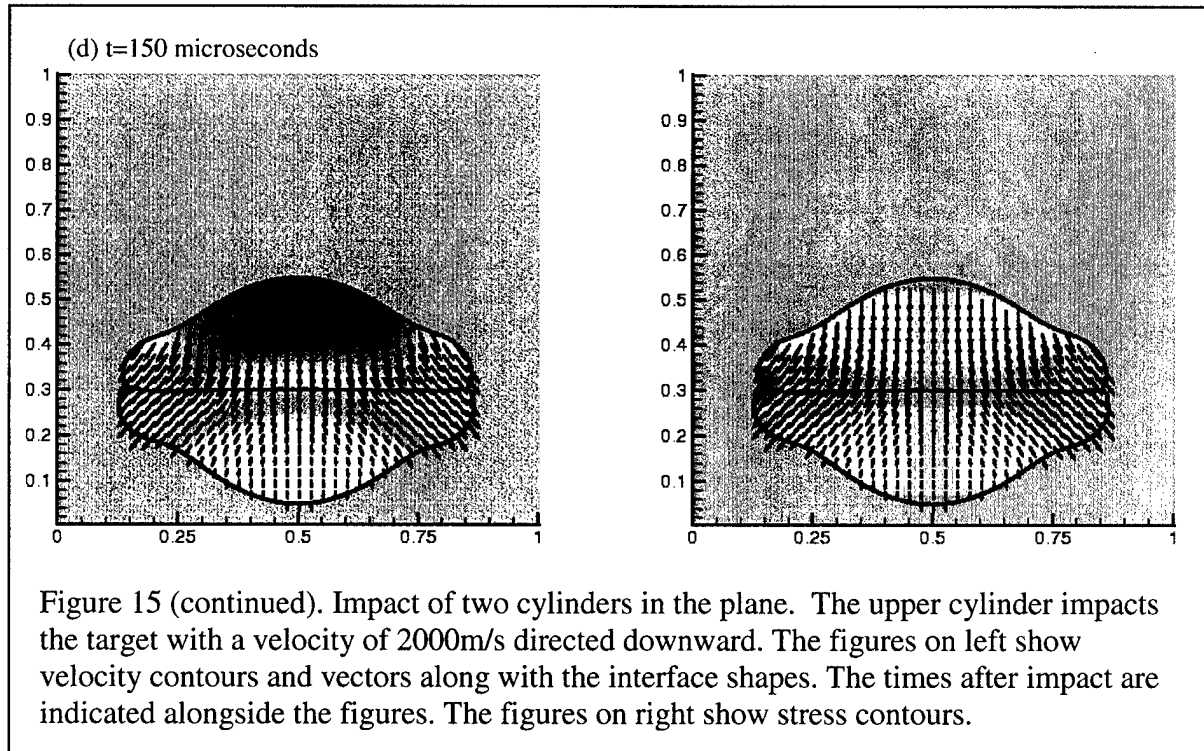


Figure 15.



In Figure 16 we show the effect of grid refinement and time step refinement on the computation of this problem. In that figure we have plotted the interfaces computed at $50 \mu\text{s}$, $75 \mu\text{s}$, $100 \mu\text{s}$ and $150 \mu\text{s}$ respectively for the following:

1. 50×50 mesh, $\text{CFL} = 0.5$
2. 100×100 mesh, $\text{CFL} = 0.5$
3. 100×100 mesh, $\text{CFL} = 0.1$

It can be seen from the figure that the solutions for these three cases are close throughout the calculation. In fact cases 2 and 3 above are almost indistinguishable due to the high-order time integration used (3rd-order). However, for $t=100 \mu\text{s}$ and $150 \mu\text{s}$ one sees differences in the solutions for the two grid resolutions. The solution for the coarser grid lags that of the finer grid. Also the largest differences appear to be at the rims of the impact area where the largest gradients are encountered due to the singular behaviour there.

As a final demonstration we simulate the impact of a projectile-like slender body with a planar target. The results are shown in Figure 17. The features of the impact process in this case are very similar to those observed before. One again sees large stress concentrations in the rim of the impact zone and the upwelling of material of the target in the region around the impact zone. This is also seen from the velocity vector plots. The direction of particle velocities reverse in the impacted material away from the impacted region leading to the upwelling of material. This is despite the specification of zero gradient conditions at all boundaries in the target which were specified to approximate the infinite extent of the target. The presence of the free surface (material-void interface) surrounding the impacted region allows for the development of a velocity at the free surface which permits the pushing and lifting of

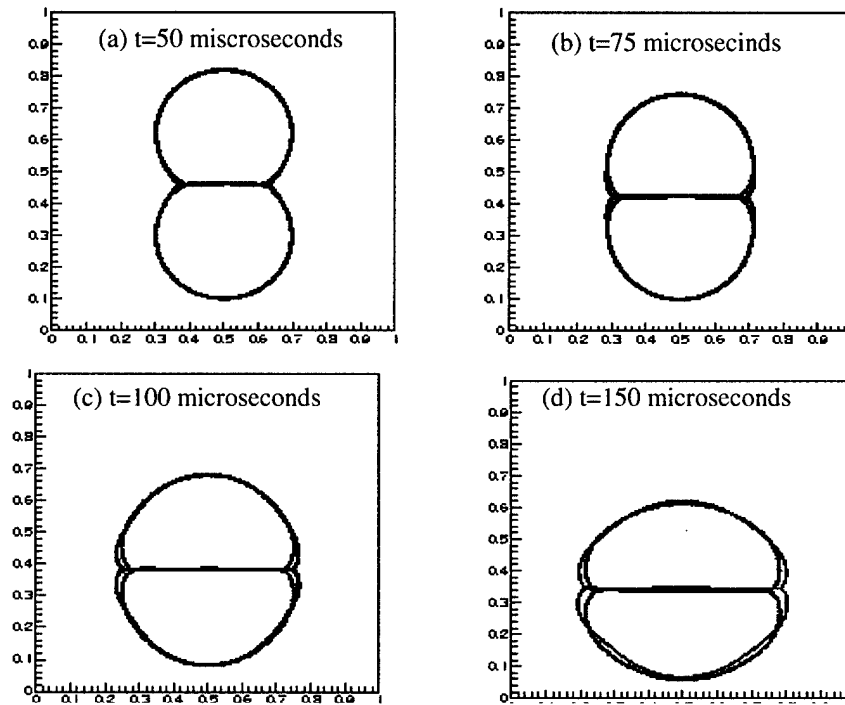
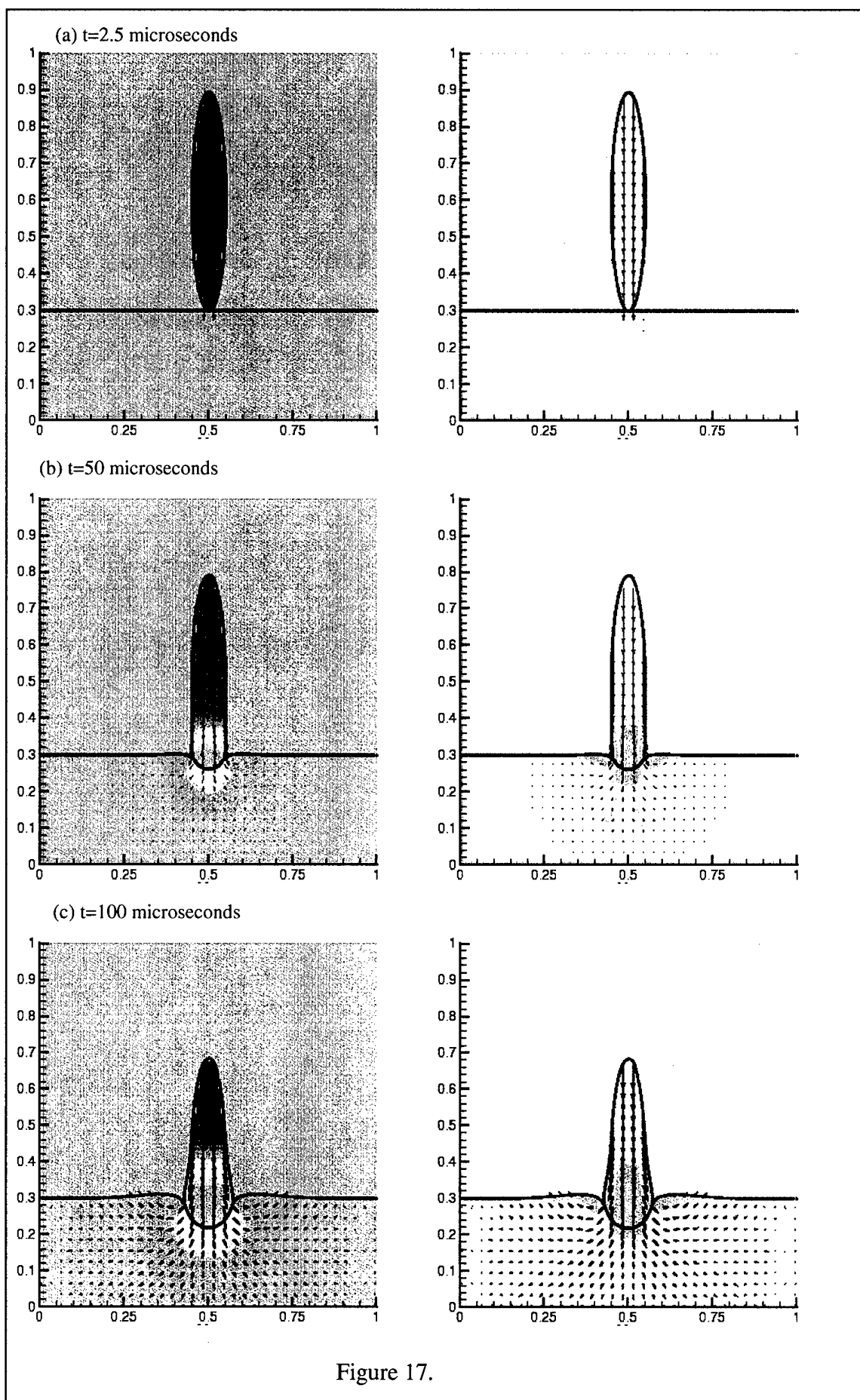


Figure 16 Grid refinement study for cylinders impacting in the plane. The interface shapes are superposed for the following cases: 50x50 mesh, CFL=0.5; 100x100 mesh, CFL=0.5; 100x100 mesh, CFL=0.1. Differences can only be discerned between the 50x50 and 100x100 mesh solutions. Interfaces for the two different time step sizes lie on each other.

material in that region. Note the shape of the crater formed due to the impact. Since the target is unconfined the resulting crater appears to be assuming a nearly circular shape.

11. Summary and future work

We have described the development of a numerical technique based on a fixed-grid sharp interface tracking approach for the simulation of multi-material impact. The physics of the problem is such that nonlinear elastic-plastic wave propagation phenomena occur in the materials leading to the formation of shocks. We track interfaces explicitly as points in 1D and curves in 2D. In its interaction with the flowfield, although we are computing on a fixed mesh, the interface is treated sharply and the discontinuities at the interface are not smeared. We have demonstrated that the current method has the following capabilities:



(d) $t=150$ microseconds

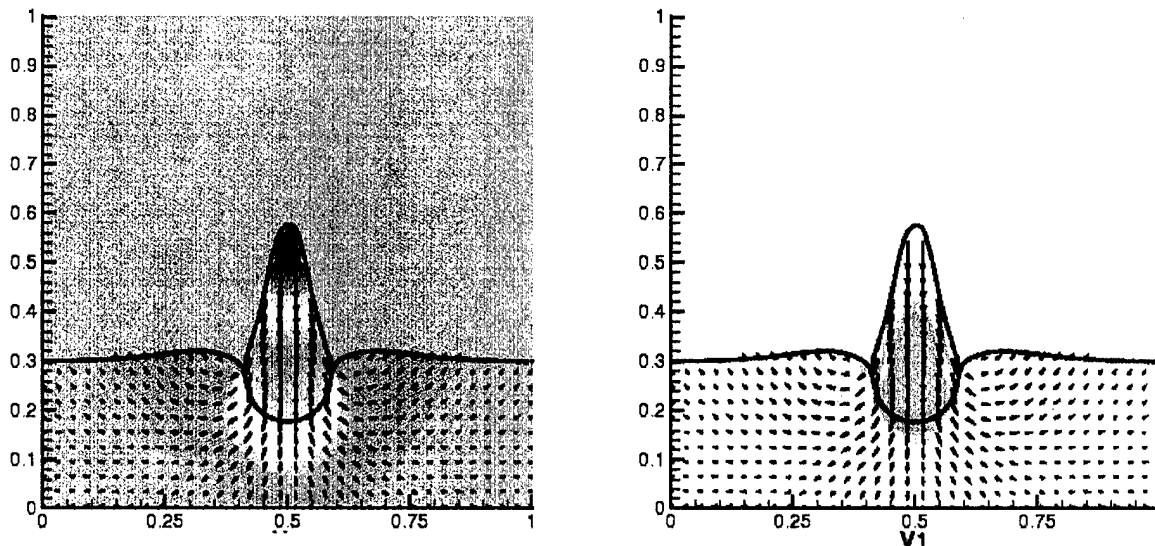


Figure 17. (Continued) Impact of a slender elliptic cylinder with a planar surface. The cylinder impacts the target with a velocity of 2000m/s directed downward. The figures on left show velocity contours and vectors along with the interface shapes. The times after impact are indicated alongside the figures. The figures on right show stress contours.

1. The interface can be tracked through large distortions.
2. Accurate shock-capturing schemes can be implemented for Cartesian grids and extended in a straightforward manner to incorporate the presence of the moving interfaces.
3. Boundary conditions are developed for the 1D uniaxial strain case and 2D plane strain case and these are applied at the exact locations of the boundaries.
4. Different regions of the boundaries can have different boundary conditions, i.e. the material-material and material-void boundary conditions. These are applied at the interface points identified to lie in regions where the interfaces are in contact and where the interface is exposed to a void, respectively. These boundary conditions are a combination of physical and numerical boundary conditions. The suitability of the set of b.c.s is determined based on numerical experimentation. The singularity resulting from an abrupt transition from a material-material to material-void b.c. at the interfaces is handled well.
5. Computations of the deformation process are carried to large distortions while the interfaces travel through the mesh in a stable and robust manner.

Future work will be directed toward establishing the validity of this method by solving problems that can be benchmarked, such as the Taylor bar impact problem in 2D. We will also work on augmenting the current capabilities by introducing grid refinement adaptively in the vicinity of interfaces and regions of large gradient. This will alleviate computational times and also enhance accuracy in desired regions thus enabling large-scale computations.

12. References

- T. Barth and J. A. Sethian, "Numerical schemes for the Hamilton-Jacobi and Level-Set equations on triangulated domains," *J. Comp Phys*, Vol. 145, pp. 1-40 (1998).
- D.J. Benson, "Computational Methods in Lagrangian and Eulerian Hydrocodes," *Comput. Methods Appl. Mech. Engrg.*, Vol. 99, pp. 235-395 (1992).
- R. P. Beyer and R. J. LeVeque, "Analysis of a one-dimensional model for the immersed boundary method," *SIAM J. Num. Anal.*, Vol. 29, No. 2, pp. 332-364 (1992).
- J. U. Brackbill, D. B. Kothe and C. Zemach, "A continuum method for modeling surface tension," *J. Comp Phys.*, Vol. 100, pp. 335-354, (1992).
- G. Caginalp, in *Applications of Field Theory to Statistical Mechanics*, Ed. Luis Garrido, Lecture Notes in Physics, No. 216, pp. 216-226, Springer-Verlag, Berlin, (1984).
- G.T. Camacho and M. Ortiz, "Computational Modeling of Impact Damage in Brittle Materials," *Int. J. Solids Structures*, Vol. 33, pp. 2899-2938 (1996).
- G.T. Camacho and M. Ortiz, "Adaptive Lagrangian Modeling of Ballistic Penetration of Metallic Targets," *Comput. Methods Appl. Mech. Engrg.*, Vol. 142, pp. 269-301 (1997).
- S. Chen, B. Merriman, S. Osher and P. Smereka, "A simple level set method for solving Stefan problems," *J. Comp. phys.*, Vol. 134, (1997).
- M. D. Dembo, D. C. Torney, K. Saxman and D. A. Hammer, "The reaction-limited kinetics of membrane-to-surface adhesion and detachment," *Proc. Roy. Soc. Lond.*, Vol. B234, pp. 55-83 (1988).
- C. Dong, R. Skalak, K.-L. P. Sung, G. W. Schmid-Schonbein and S. Chien, "Passive deformation analysis of human leukocytes," *J. Biomech. Eng.*, Vol. 110, pp. 27-36 (1988).
- A. Duarte and J. T. Oden, "An h-p adaptive method using clouds," *Comput. Methods Appl. Mech. Engrng.*, Vol. 139, pp. 237-262 (1996).
- L. J. Fauci, and C. S. Peskin, "A computational model of aquatic animal locomotion," *J. Comp. Phys.* **77**, pp. 85-108 (1988).
- M. J. Fritz and J. P. Boris, "The Lagrangian solution of transient problems in hydrodynamics using a triangular mesh," *J. Comp. Phys.*, Vol. 31, pp. 173-215 (1979).

- J. Glimm, J. Grove, B. Lindquist, O. A. McBryan, and G. Tryggvason, "The bifurcation of tracked scalar waves," *SIAM J. Sci. Stat. Comput.* Vol. 1, pp. 61-79 (1988).
- R. Glowinski, T.-S. Pan and J. Periaux, "A fictitious domain method for Dirichlet problem and applications," *Comp. Meth. Appl. Mech. Eng.*, Vol. 111, pp. 283-303 (1994).
- D. Goldstein, R. Handler, and L. Sirovich, "Modeling a no-slip surface with an external force field," *J. Comput. Phys.* Vol. 105, pp. 354-366 (1993).
- D. Goldstein, R. Handler, and L. Sirovich, "Direct numerical simulation of turbulent flow over a modeled riblet covered surface," *J. Fluid Mech.* Vol. 302, pp. 333-376 (1995).
- A. Harten, B. Engquist, S. Osher and S. R. Chakravarthy "Uniformly high-order accurate essentially non-oscillatory schemes, III," *J. Comp Phys*, Vol. 131, pp. 3-47 (1997).
- C. W. Hirt, and B. D. Nichols, "Volume of Fluid (VOF) method for the dynamics of free boundaries," *J. Comp. Phys.* Vol. 39, pp. 201-225 (1981).
- T. Y. Hou, Z. Li, S. Osher and H. Zhao, "A hybrid method for moving interface problems with application to the Hele-Shaw flow," *J. Comp. Phys.*, Vol. 134, No.2, pp. 236-351 (1997).
- V. Jayaraman, H. S. Udaykumar and W. Shyy, "Adaptive unstructured grid for three-dimensional interface representation," *Num. Heat Transf.*, Part B, Vol. 32, 247-265 (1997).
- G.-S. Jiang and C.-W. Shu, "Efficient implementation of weighted ENO schemes," *J. Comp Phys*, Vol. 126, pp. 202-228 (1996).
- R. A. Johnson and D. M. Belk, "Multigrid approach to overset grid communication," *AIAA J.*, Vol. 33, 2305-2308 (1995).
- D. A. Jones, C. W. Smith and L. V. McIntire, "Effects of fluid shear stress on leukocyte adhesion to endothelial cells," in *Physiology and Pathophysiology of Leukocyte Adhesion*, 148, Oxford University Press, New York.
- D. Juric, and G. Tryggvason, "A front tracking method for dendritic solidification," *J. Comp. Phys.* Vol. 123, pp. 127-148 (1996).
- H.-C. Kan, H. S. Udaykumar, W. Shyy and R. Tran-Son-Tay, "Hydrodynamics of a compound drop with application to leukocyte modeling," *Phys. Fluids*, Vol 10, No. 4, pp. 760-774 (1998).
- A. Karma and W.-J. Rappel, "Numerical simulation of three-dimensional dendrite growth," *Phys. Rev Letters*, Vol. 77, No. 19, pp. 4050-4053 (1996).
- R. Kobayashi, "Modeling and numerical simulation of dendritic crystal growth," *Physica D*, Vol. 63, pp. 410-423, (1993).
- D. B. Kothe and R. C. Mjolsness, "Ripple: A new model for incompressible flows with free surfaces," *AIAA Journal*, Vol. 30, pp. 2694-2700, (1992).
- R. J. LeVeque, "*Numerical Methods for Conservation Laws*," Birkhauser, Boston (1990).

- R. J. LeVeque and Z. Li, "The immersed boundary method for elliptic equations with discontinuous coefficients and singular sources," *SIAM J. Num. Anal.*, Vol. 31, No. 4, pp. 1019-1044 (1994).
- T. J. Lizska, C. A. M. Duarte and W.W. Tworzydlo, "hp-Meshless cloud method," *Comput. Methods Appl. Mech. Engrng.*, Vol. 139, pp. 263-288 (1996).
- J. E. Melton, F. Y. Enomoto and M. J. Berger, "3D automatic grid generation for Euler flows," *AIAA 93-3386-CP* (1993).
- M.A. Meyers, "*Dynamics Behavior of Materials*," John Wiley & Sons Inc., New York (1994).
- S. Osher, and J. A. Sethian, "Fronts propagating with curvature dependent speed: Algorithms based in Hamilton-Jacobi formulations," *J. Comp. Phys.*, Vol 79, pp. 12-49(1988).
- R. B. Pember, J. B. Bell, and P. Colella, "An adaptive Cartesian grid method for unsteady compressible flow in irregular regions," *J. Comp. Phys.*, Vol. 120, pp. 278-304 (1995).
- C. S. Peskin, "Numerical analysis of blood flow in the heart," *J. Comp. Phys.*, Vol. 25, pp. 220-252 (1977).
- J. J. Quirk, "An alternative to unstructured grids for computing gas dynamic flows around arbitrarily complex two-dimensional bodies," *ICASE Report No. 92-7*, NASA Langley Research Center, Hampton, VA (1992).
- P. W. Randles and L. D. Libersky, "Smoothed particle hydrodynamics: some recent improvements and applications," *Comput. Methods Appl. Mech. Engrng.*, Vol. 139, pp. 375-408 (1996).
- R. D. Rausch, J. T. Batina and H. T.Y. Yang, "Three-dimensional time-marching aeroelastic analyses using an unstructured-grid Euler method," *AIAA J.*, Vol. 31, No. 9, pp. 1626-1633 (1993).
- R. Scardovelli and S. Zaleski, "Direct numerical simulation of free-surface and interfacial flow," *Ann. Rev. Fluid Mech.*, to be published (1999).
- A. Schmidt, "Computation of three dimensional dendrites with finite elements," *J. Comp Phys*, Vol 125, pp. 293-312 (1996).
- J. A. Sethian, *Level Set Methods: Evolving interfaces in geometry, fluid mechanics, computer vision, and materials science*, Cambridge University Press (1996).
- C.-W. Shu, and S. Osher, "Efficient implementation of essentially non-oscillatory shock-capturing schemes," *J. Comp Phys*, Vol. 77, pp. 439-471 (1988).
- C.-W. Shu and S. Osher, "Efficient implementation of essentially non-oscillatory shock-capturing schemes II," *J. Comp Phys*, Vol. 83, pp. 32-78 (1989).
- W. Shyy, "*Computational Modeling for Fluid Flow and Interfacial Transport*," Elsevier, Amsterdam, The Netherlands (1994).
- W. Shyy, H. S. Udaykumar, M. M. Rao, and R. W. Smith, *Computational Fluid Dynamics with Moving Boundaries*, Hemisphere, Washington, D.C. (1996).

- R. W. Smith and W. Shyy, "Computation of aerodynamic coefficients for a flexible membrane airfoil in turbulent flow: A comparison with classical theory," *Phys. Fluids*, Vol. 8, pp. 3346-3353 (1996).
- J. Snyder and A. R. Woodbury, "Interval methods for multi-point collisions between time-dependent curved surfaces," *Comput. Graphics Proceedings, Annual Conference Series, SIGGRAPH 93*, pp. 321-334 (1993).
- J. L. Steger, "Thoughts on the Chimera grid method of simulation of three-dimensional viscous flow," *Proc. Computational Fluid Dynamics Symposium on Aeropropulsion*, NASA CP -3078, pp. 1-10 (1991).
- M. Sussman, A. S. Almgren, J. B. Bell, P. Collela, L. H. Howell, M. L. Welcome, "An adaptive level set approach for incompressible two-phase flows," Lawrence Berkely Laboratory Report, LBNL-40327 (1997).
- J.A. Trangenstein, "A Second-Order Algorithm for the Dynamic Response of Soils," *Impact of computing in Science and Engineering*, Vol. 2, pp. 1-39 (1990).
- J.A. Trangenstein, "A Second-Order Algorithm for Two-Dimensional Solid Mechanics," *Comput. Mech.*, Vol. 13, pp. 343-359 (1994).
- J.A. Trangenstein, "Adaptive Mesh Refinement for Wave propagation in Nonlinear Solids," *SIAM J. Sci. Comput.*, Vol. 16, pp. 819-939 (1995).
- J.A. Trangenstein and R.B. Pember, "The Riemann Problem for Longitudinal Motion in an Elastic-Plastic Bar," *SIAM J. Sci. Stat. Comput.*, Vol. 12, pp. 180-207 (1991).
- C. Tu and C. S. Peskin, "Stability and instability in the computation of flows with moving immersed boundaries: a comparison of three methods," *SIAM J. Sci. Stat. Comput.*, Vol. 13, pp. 1361-1376 (1992).
- H. S. Udaykumar, and W. Shyy, "A grid-supported marker particle scheme for interface tracking," *Num. Heat Transf. B*, Vol. 27, pp. 127-153 (1995a).
- H. S. Udaykumar, and W. Shyy, "Simulation of morphological instabilities during solidification; part I: conduction and capillarity effects," *Int. J. Heat Mass Transf.*, Vol. 38, pp. 2057-2073 (1995b).
- H. S. Udaykumar, W. Shyy and M. M. Rao,, "ELAFINT - A mixed Eulerian-Lagrangian method for fluid flows with complex and moving boundaries," *Int. J. Numer. Meth. Fluids.*, Vol. 22, pp. 691-704 (1996).
- H. S. Udaykumar, H-C. Kan, W. Shyy and R. Tran-Son-Tay, "Multiphase dynamics in arbitrary geometries on fixed Cartesian grids," *J. Comp Phys.*, Vol. 137, pp. 366-405 (1997).
- H. S. Udaykumar, R. Mittal, W. Shyy,"Computation of solid-liquid phase fronts in the sharp interface limit on fixed grids," *J. Comp Phys.*, Vol. 153, pp. 535-574 (1999).
- S. O. Unverdi, and G. Tryggvason, "A front tracking method for viscous, incompressible, multi-fluid flows," *J. Comp. Phys.*, Vol. 100, pp. 25-37 (1992).

- K. J. Vanden, "Characteristic analysis of the uniaxial stress and strain governing equations with thermal-elastic and Mie-Gruneisen equation of state," Technical Memorandum, AFRL, Eglin AFB, Eglin, FL (1998).
- V. Venkatakrishnan, "Perspectives on unstructured grid flow solvers," *AIAA J.*, Vol. 34, pp. 533-547 (1996).
- V. R. Voller and C. Prakash, "A fixed grid numerical modeling methodology for convection-diffusion mushy region phase-change problems," *Int. J. Heat Mass Transf.*, Vol. 30, pp. 1709-1719 (1987).
- A. A. Wheeler, W. J. Boettinger and G. B. McFadden, "Phase field model for isothermal phase transitions in binary alloys," *Phys. Rev. A*, Vol. 45, pp. 7424-7439 (1992).
- T. Ye, R. Mittal, H. S. Udaykumar and W. Shyy, "A Cartesian grid method for simulation of viscous incompressible flow with complex immersed boundaries," *AIAA99-3312*, also accepted for publication in *J. Comp Physics*. (1999)
- D. P. Young, R. G. Melvin, M. B. Bieterman, F. T. Johnson, S. S. Samant, and J. E. Bussoletti, "A locally refined rectangular grid finite element method: Application to computational fluid dynamics and computational physics," *J. Comp. Phys.*, Vol. 92, pp. 1-66 (1992).
- D. D. Zeeuw, and K. G. Powell, "An adaptively-refined Cartesian mesh solver for the Euler equations," *AIAA Paper No. 90-0000* (1990).
- H. Zhang, L. L. Zheng, V. Prasad, T. Y. Hou, "A curvilinear level set formulation for highly deformable free surface problems with application to solidification," *Num. Heat Transf., Part B*, Vol. 34, pp. 1-20, (1998)

DISTRIBUTION LIST
AFRL-MN-EG-TR-2000-7005

Defense Technical Information Center	1
8725 John J. Kingman Road, Ste 0944	
Ft Belvoir, VA 22060-6218	

Air University Library	1
600 Chennault Circle	
Bldg 1405	
Maxwell AFB, AL 36112-6424	

EGLIN AFB OFFICES:

AFRL/MN/CA-N	1
AFRL/MNOC-1 (STINFO Office)	1
AFRL/MNA	1
AFRL/MNAC	1